

National Technical University of Athens
School of Chemical Engineering
Department of Materials Science and Engineering
Computational Materials Science and Engineering Group (Co.M.S.E)

Molecular Dynamics Study of Homogeneous Nucleation in Linear Polyethylene Under Flow-Induced and Quiescent Conditions

Master's Thesis

by

Konstantinos Vasileios Psillos

A Thesis submitted in partial fulfillment of the Joint Postgraduate Program "Computational Mechanics"

Supervisor: Doros Nicolas Theodorou,Professor NTUA

Athens, June 2025

National Technical University of Athens,School of Chemical Engineering
Konstantinos Vasileios Psillos

Abstract

Molecular simulation has become a very powerful tool for understanding the process of polymer crystallization. By using carefully constructed simulations, one can observe the two phenomena responsible for melt crystallization: nucleation and growth. This work used Molecular Dynamics (MD) simulations with a united atom force field, which is well-parameterized for PE, to study homogeneous crystal nucleation in linear polyethylene (PE) melts under quiescent and flow-induced conditions. In order to study the effect of molecular weight on crystallization kinetics, two polydisperse PE systems were constructed using a home-built Monte Carlo sampling procedure with a uniform chain length selection. The first system consisted of 50 PE chains with an average length of 2,000 CH_2 units per chain, while the second consisted of 100 chains with an average length of 1,000 CH_2 units per chain. A drawing (stretching) protocol mimicking an industrial process of uniaxial deformation was applied for the flow-induced case, while a quiescent isothermal protocol was used as a control.

The progress of crystallization was quantified using a home-built algorithm to estimate the evolution of the degree of crystallinity over time, and important kinetic parameters were determined through a mean first-passage time analysis (MFPT). In particular, we observe that flow dramatically accelerates nucleation. The induction time τ^* under flow-induced conditions is on the order of tens of nanoseconds, whereas under quiescent conditions τ^* is an order of magnitude longer. On the other hand, the critical nucleus size n^* in both crystallization protocols remains almost the same ($\approx$ 100 CH_2 units), indicating that flow accelerates crystallization, without significantly altering the thermodynamics of the critical cluster size.

Furthermore, we show that, within the studied molecular weight range, chain length has minimal impact on nucleation. Both systems exhibit nearly identical induction times and critical nucleus sizes under the same crystallization conditions. It should be noted that all simulations were carried out at temperature $T = 340$K, about 15% subcooling.

Overall, our results are in qualitative agreement with prior experimental observations and similar MD studies, providing molecular-level insights, which are valuable for understanding and optimizing polymer processing.

Keywords:

Molecular Dynamics (MD), Polymer Crystallization, Nucleation Kinetics, MFPT Analysis

Περίληψη

Οι ατομιστικές προσομοιώσεις αποτελούν ένα πολύ χρήσιμο εργαλείο για την κατανόηση της κρυστάλλωσης των πολυμερών. Σχεδιάζοντας κατάλληλες προσομοιώσεις, μπορεί κανείς να μελετήσει τα δύο φαινόμενα που διέπουν την κρυστάλλωση των πολυμερικών τηγμάτων: την πυρηνοποίηση και τη μετέπειτα ανάπτυξη των κρυστάλλων. Στην παρούσα μεταπτυχιακή εργασία, χρησιμοποιήθηκε η μέθοδος της Μοριακής Δυναμικής με την χρήση εμπειρικού δυναμικού ενοποιημένων ατόμων, το οποίο είναι σωστά παραμετροποιημένο για το πολυαιθυλένιο, ώστε να μελετηθεί η κρυστάλλωση τηγμάτων πολυαιθυλενίου υπό συνθήκες ηρεμίας (απουσία ροής) και εξωτερικά επιβαλλόμενης ροής. Ακόμη, για να μελετηθεί η επίδραση του μοριακού βάρους στην κινητική της κρυστάλλωσης, κατασκευάστηκαν δύο πολυδιάσπαρτα τήγματα πολυαιθυλενίου. Το πρώτο αποτελείται από 50 αλυσίδες πολυαιθυλενίου με μέσο μήκος 2.000 ατόμων άνθρακα ανά αλυσίδα, ενώ το δεύτερο αποτελείται από 100 αλυσίδες πολυαιθυλενίου με μέσο μήκος 1.000 ατόμων άνθρακα ανά αλυσίδα. Στην περίπτωση της εξωτερικά επιβαλλόμενης εκτατικής ροής, ακολουθήθηκε ένα πρωτόκολλο επιμήκυνσης που μιμείται μια βιομηχανική διαδικασία μηχανικού προσανατολισμού, ενώ στην περίπτωση της απουσίας ροής ακολουθήθηκε ένα ισόθερμο πρωτόκολλο.

Η εξέλιξη της κρυστάλλωσης ποσοτικοποιήθηκε με τη χρήση ενός αλγορίθμου που εκτιμά την εξέλιξη του βαθμού κρυσταλλικότητας με την πάροδο του χρόνου, και προσδιορίσθηκαν σημαντικές κινητικές παράμετροι της κρυστάλλωσης μέσω της μεθόδου μέσου χρόνου μέσης διάβασης. Πιο συγκεκριμένα, παρατηρήθηκε ότι η κρυστάλλωση υπό συνθήκες ροής επιτυγχάνεται σημαντικά πιο γρήγορα σε σχέση με την κρυστάλλωση υπό συνθήκες ηρεμίας. Ο χρόνος επαγωγής υπό συνθήκες ροής είναι της τάξεως δεκάδων νανοδευτερολέπτων, ενώ υπό συνθήκες ηρεμίας, ο χρόνος αυτός υπολογίζεται μία τάξη μεγέθους μεγαλύτερος. Αναφορικά με το κρίσιμο μέγεθος πυρήνα, και στα δύο πρωτόκολλα κρυστάλλωσης, αυτό παραμένει σχεδόν σταθερό, δείχνοντας ότι είναι πιθανόν η θερμοδυναμική της δημιουργίας του κρίσιμου πυρήνα να μην επηρεάζεται σημαντικά από τα πρωτόκολλα κρυστάλλωσης.

Ακόμη, εντός του μελετώμενου εύρους μοριακών βαρών, το μήκος των αλυσίδων έχει ελάχιστη επίδραση στη δημιουργία των πυρήνων. Τα δύο συστήματα εμφανίζουν πανομοιότυπους χρόνους επαγωγής και κρίσιμα μεγέθη πυρήνων υπό τις ίδιες συνθήκες κρυστάλλωσης.

Συμπερασματικά, τα αποτελέσματα της συγκεκριμένης μεταπτυχιακής εργασίας είναι ποιοτικά σύμφωνα με προηγούμενες δημοσιευμένες πειραματικές και υπολογιστικές μελέτες, παρέχοντας

έτσι πληροφορίες που είναι πολύτιμες για την κατανόηση και τη βελτιστοποίηση διαδικασιών επεξεργασίας πολυμερών.

Λέξεις-κλειδιά:
Μοριακή Δυναμική (ΜΔ), Κρυστάλλωση Πολυμερικών Τηγμάτων, Κινητική της Κρυστάλλωσης

Acknowlegdements

I conducted this thesis as a member of the Computational Material Science and Engineering (Co.M.S.E) Group in the School of Chemical Engineering at NTUA. Now that the thesis is completed, I would like to express my sincere gratitude to those who assisted and supported me towards its completion

First and foremost, I would like to start by expressing my sincerest gratitude to my academic adviser, **Professor Doros Theodorou**, the person who entrusted me with this project and gave me the opportunity to work with him. His commitment to scientific research and education has been an invaluable motivating force for me.

I am also deeply grateful to **Dr. Stefanos Anogiannakis** (post-doctoral researcher) and **Mr. Fotis Venetsanos** (PhD candidate) for their constant assistance, insightful discussions, and advice during my work; without their expertise and day-to-day help, this thesis would not have been possible.

Furthermore, I want to express my gratitude to my parents for their unwavering support and belief in me throughout this journey.

I would also like to thank my friends from the Computational Mechanics master's program-Charis, Dimitris, and Kyriakos- for their friendship and encouragement.

Finally, I acknowledge the supportive environment of the Co.M.S.E. research group and the facilities provided by NTUA, which were essential to the success of this work.

Contents

Abstract ii

Περίληψη iv

Acknowledgements vi

1 Introduction 1
- 1.1 Introduction to Semicrystalline Polymers . . . 1
- 1.2 The Challenge of Recycling . . . 2
- 1.3 Monomaterial Packaging . . . 2
- 1.4 Morphology of Semicrystalline Polymers . . . 4
  - 1.4.1 Microscopic Structure: Lamellae and Tie Molecules . . . 4
  - 1.4.2 Spherulitic Superstructure . . . 4
- 1.5 Polymer Crystallization . . . 5
- 1.6 Thesis Objective . . . 7

2 Fundamentals of Homogeneous Crystal Nucleation 8
- 2.1 Introduction to PE crystallization . . . 8
- 2.2 Nucleation Theories . . . 9
  - 2.2.1 Classical Nucleation Theory (CNT) . . . 9
  - 2.2.2 Limitations of CNT for Polymers . . . 11
  - 2.2.3 Density Functional Theory (DFT) . . . 12
- 2.3 Experimental Studies on PE Nucleation . . . 13
  - 2.3.1 Differential Scanning Calorimetry (DSC) . . . 13
  - 2.3.2 Polarizing Optical Microscopy (POM) . . . 14
  - 2.3.3 Synchrotron X-ray Scattering (SAXS/WAXS) . . . 15
- 2.4 Computational Studies of PE Nucleation . . . 16
  - 2.4.1 Molecular Dynamics (MD) Simulations . . . 16
  - 2.4.2 Monte Carlo (MC) . . . 17
  - 2.4.3 Key Insights from Simulations . . . 18

3 Fundamentals of Molecular Simulations 19

3.1 Statistical Mechanics and Ensembles . . . 19
3.1.1 Basics of Statistical Mechanics . . . 19
3.1.2 Ensemble Theory and MD . . . 22
3.2 Monte Carlo (MC) Method . . . 24
3.2.1 Principles of Monte Carlo Simulations . . . 24
3.2.2 Monte Carlo-Driven Equilibration for Molecular Dynamics Simulations 25
3.3 Fundamentals of MD Simulations . . . 27
3.3.1 Newtonian Mechanics . . . 27
3.3.2 Integration of Equation of Motion: The leap-frog Algorithm . . . 27
3.3.3 System Initialization . . . 28
3.3.4 Energy Minimization . . . 28
3.3.5 Periodic Boundary Conditions (PBC) . . . 29
3.4 Force Field and Computational Efficiency . . . 30
3.4.1 Bonded Interactions . . . 30
3.4.2 Non-Bonded Interactions . . . 30
3.4.3 Other Force Fields for PE Melts . . . 31
3.5 Neighbor Lists and Computational Efficiency . . . 31

4 Methodology 32
4.1 System Studied . . . 32
4.2 Pre-Processing Protocol . . . 33
4.3 Simulation Protocol . . . 33
4.3.1 Quiescent Conditions . . . 34
4.3.2 Flow-induced Conditions . . . 34
4.4 Post-Processing Protocol . . . 34
4.4.1 Estimation of Degree of Crystallinity . . . 34
4.4.2 Kinetic Analysis . . . 36

5 Results & Discussion 38
5.1 System of 50 C2000 chains . . . 38
5.1.1 Degree of Crystallinity . . . 38
5.1.2 Kinetic Analysis . . . 42
5.1.3 Nucleation Rate Calculations . . . 45
5.1.4 Estimation of Induction Time from Probability Distributions of Nucleation Times . . . 46
5.1.5 Time Evolution of the Chain Root Mean Squared Radius of Gyration 48
5.1.6 Crystallization Visualization . . . 50
5.2 Molecular Weight Effects on Crystallization: 1K vs. 2K Systems . . . 54
5.2.1 Flow-Induced Conditions . . . 54
5.2.2 Quiescent Conditions . . . 55
5.2.3 MFPT-Derived Kinetic Parameters . . . 57

6 Conclusion &Future Work **58**
6.1 Conclusion 58
6.2 Future Work 59
6.2.1 Effect of Higher Temperature (Lower Subcooling) 59
6.2.2 Varying Flow Strength and Partial Alignment 59
6.2.3 Effect of Larger Dispersities and Molecular Architecture 59

Bibliography **66**

List of Figures

1.1 Distribution of the global plastic use by application.[1] 3

1.2 Hierarchical structure of semicrystalline polymers illustrating chain folds, lamellae, and spherulitic formations.[2] 5

1.3 Stages of crystallization in polymers, showing the transition from a homogeneous polymer melt (left) to a fully crystallized structure (right).[3] 6

2.1 Illustration of ΔG versus N, where A represents the surface area of the nucleus. There are notable variations in the size and shape of the nano-nucleus. Δg is associated with critical nano-nucleation, which serves as the activation barrier.[4] 10

3.1 Schematic Representation of microcanonical (NVE), canonical (NVT) and isothermal-isobaric (NPT) statistical ensembles [5]. 22

3.2 Schematic Representation of different levels of coarse-graining [6] 26

3.3 Schematic of the leap-frog method. Positions are evaluated at integer time steps, while velocities are evaluated at half-integer steps [7]. 27

3.4 The central simulation box (outlined in black) is surrounded by periodic image boxes. When a particle (red or blue sphere) leaves one side of the primary box, it re-enters from the opposite side (blue arrows indicate the trajectory of a moving particle). Thus, each molecule always finds a neighbor even at the boundaries, as it effectively interacts with an infinite array of images [8]. . . 29

4.1 Time evolution of the degree of crystallinity X_c using three different methods: Yamamoto's orientational-based method (black line), density-based definition (red line), and thermodynamic enthalpy-based definition (blue line). The plot corresponds to one 2K PE system, which is drawn at a constant strain rate of $\dot{\varepsilon} = 10^7\ \mathrm{s}^{-1}$ at $T = 340\,\mathrm{K}$. 36

5.1 Time evolution of the degree of Crystallinity X_c from 10 independent MD simulations of polydisperse 2K PE system under stretching conditions. . . . 39

5.2 Mean crystallization curve $X_c(t)$ for the polydisperse 2K PE system under stretching conditions, calculated as the average of 10 independent MD simulation runs. The curve exhibits a characteristic sigmoidal shape: an initial lag (induction period), followed by a steep rise as crystallization proceeds, and finally a plateau. 39

5.3 Time-resolved crystallinity trajectories $X_c(t)$ from 20 independent MD simulations of polydisperse 2K PE system under quiescent conditions. Each $X_c(t)$ reflects the stochastic nature of homogeneous nucleation, with the induction time for nucleation varying significantly across runs. 41

5.4 Average crystallization curve $X_c(t)$ for the polydisperse 2K PE system under quiescent conditions, derived from the trajectories in Figure 5.3. 41

5.5 The mean first-passage time (MFPT) of the maximum nucleus size $n_{\max}$ for 10 MD simulations of a system of 50 polydisperse PE chains quenched from 450 K to 340 K and then stretched (flow-induced crystallization). The open circles represent the simulation MFPT data points, and the solid red line corresponds to the fitted MFPT theoretical curve. Error bars represent the standard error of the mean (SEM) of the passage time for each $n_{\max}$. 43

5.6 The mean first-passage time (MFPT) of the maximum nucleus size $n_{\max}$ for 20 MD simulations of a system of 50 polydisperse PE chains quenched from 450 K to 340 K. The open circles represent the simulation MFPT data points, and the solid red line corresponds to the fitted MFPT theoretical curve. Error bars represent the standard error of the mean (SEM) of the passage time for each $n_{\max}$. 44

5.7 Obtained probability distribution P(t) of the induction time for 2K system in flow-induced conditions. The red solid line is a fit of the theoretical equation to the simulation data, while the open circles represent the binned values of nucleation times determined from MFPT analysis for each independent simulation (10 independent simulations). The error bars represent the standard error of each bin, estimated as $\sqrt{n}/N$, where n is the number of events in the bin and $N = 10$ is he number of independent simulations. 47

5.8 Obtained probability distribution P(t) of the induction time for 2K System in quiescent conditions. The red solid line is a fit of the theoretical equation to the simulation data, while the open circles represent the nucleation times determined from MFPT analysis for each independent simulation (20 independent simulations). 48

5.9 Time-dependent behavior of the chain root mean squared radius of gyration (black curve) and the simulation cell length along the Y-direction (red curve) for a 2K (C2000) PE system of polydispersity 1.08 crystallizing under flow-induced conditions at 340 K. The results shown are from one independent simulation. 49

5.10 Time-dependent behavior of the chain root mean squared radius of gyration (black curve) and the simulation cell length along the X-, Y-, and Z-direction (red, blue and green curve, accordingly) for a 2K (C2000) PE system of polydispersity 1.08 crystallizing under flow-induced conditions at 340 K. The results shown are from one independent simulation. 49
5.11 Chain root mean squared radius of gyration (black curve) and simulation cell length along the X-direction (red curve) for a 2K (C2000) PE system of polydispersity 1.08 in the absence of flow at 340 K. The results shown are from one independent simulation. 50
5.12 Initial configuration of the 2K PE system at $t \approx 0$ ns after quenching to 340 K under flow-induced conditions. Pink amorphous regions ($P_2 < 0.7$). . . . 51
5.13 Emergence of a critical nucleus at $t \approx \tau^*$ during uniaxial elongation ($\dot{\varepsilon} = 10^7$ s^{-1}) of the 2K PE system. Cyan crystalline regions ($P_2 > 0.7$) 51
5.14 Intermediate crystallization stage under flow. 52
5.15 Final oriented semi-crystalline morphology ($t = 200$ ns) under flow-induced conditions. 52
5.16 Initial amorphous configuration of the 2K PE system under quiescent conditions at $t = 0$ns (340K). Pink amorphous regions ($P_2 < 0.7$). 53
5.17 Critical nucleus formation at $t \approx 240$ns in quiescent crystallization. Cyan crystalline regions ($P_2 > 0.7$) 53
5.18 Intermediate crystallization stage under quiescent conditions. 53
5.19 Final semi-crystalline morphology from quiescent crystallization. Multiple independent crystals (cyan) with random crystallographic orientations are formed by the end of the simulation. 54
5.20 Time evolution of the degree of Crystallinity X_c from 21 independent MD simulations of polydisperse 1K PE system under stretching conditions. Flow significantly reduces the induction time and narrows trajectory dispersion compared to quenching. 55
5.21 Time-resolved crystallinity trajectories $X_c(t)$ from 23 independent MD simulations of polydisperse 1K PE system under quiescent conditions. Each $X_c(t)$ reflects the stochastic nature of homogeneous nucleation, with the induction time for nucleation varying significantly across runs. 56

Chapter 1

Introduction

1.1 Introduction to Semicrystalline Polymers

The production and consumption of plastics have had a meteoric rise, from being nearly non-existent in the early 20th century to an annual production of over 410 million metric tons today [1]. This rapid increase of plastics and, therefore, their extensive use is more than obvious in all of everyday life, and it is undoubtedly no coincidence as their success relies on a rare duality, that is, being either flexible or rigid depending on the process they have undergone and the purpose they will serve [9].

While technically "plastic" encompasses any deformable material, over 90% of plastics used industrially today are synthetic polymers–hydrocarbon-based macromolecules. These polymers are formed when monomers (simple molecules like ethylene or propylene) chemically bond, creating repeating chains or branched frameworks [10]. Imagine a molecular-scale assembly line: identical units link together, forming structures that range from linear strands, like supermarket bags, to cross-linked networks found in epoxy resins. On a larger scale, these chains interwine into disordered, glue-like matrices, the flexibility and strength of which depend on bonding patterns and molecular alignment.

One subset that is both crucial and widespread, semicrystalline polymers, dominates industries including packaging and automobile manufacture. For instance, polyethylene (PE), the most ubiquitous semicrystalline polymer is a paradox in materials science: molecular simplicity underpinning vast industrial utility [11]. Structurally, PE is little more than repeating ethylene (–CH_2–CH_2–) units linked into chains–a design so elementary [12]. A large percentage of the annual plastic production is dominated by PE, which feeds into uses ranging from everyday grocery bags to life-saving bulletproof vests, all made possible by controlling its semicrystalline architecture.

1.2 The Challenge of Recycling

Even since the 1950s, plastic manufacturing has risen continuously, thus posing some severe environmental challenges. Plastic production globally reached more than 8,300 million metric tons by 2015, but the recycling systems that had been developed by then could not address such a large quantity–only 12% of annual plastic waste was recycled until the year 2016 [13, 14, 15]. Industrial production has entirely avoided the massive and destructive effects on the environment without taking any steps to prevent it until now, when environmental hazards such as oceanic microplastic pollution and the toxicity of incinerators have posed a real threat to the environment and human life. Each year, tens of millions tons of plastic waste are disposed in landfills, polluting the soil and groundwater, and activities such as dumping of wastes in the ocean, prohibited since 1990 [16], show how previous generations have once managed the environment.

China's ban on plastic imports in 2017 broke the usual arrangement [17]. The U.S., Germany, and other countries had to tackle an extremely difficult situation due to large quantities of plastic, as already overflowing landfills [18] discharge poisonous and highly toxic materials and have no more room to expand. Incinerators [19], which are promoted for the purpose of energy recovery, pollute the air of low-income people. These stop-gap measures do not address the core problem: a broken system that treats plastic as waste and not as a resource.

Moreover, the two main recycling methods, chemical [20] and mechanical [21], have not managed to address and deal with the problem as they have specific drawbacks. More specifically, the chemical method of pyrolysis [22] is based on breaking plastics into raw chemicals, but it consumes energy and may lead to contaminated feedstocks. PET plastic, such as the one used in water bottles, can reach 90% purity [23], but along with dyes, plasticizers, or layered composites–inhibits the process. In a similar way, mechanical recycling has its disadvantages as it grinds waste into pellets, but it is inhibited by mixed streams. Imagine shredding grocery bags (polyethylene) with the labels being PVC or chip bags (PET fused to nylon)–current tech can't untangle this mess. Each melting cycle degrades plastics, turning bottles into park benches and then landfill filler.

1.3 Monomaterial Packaging

Packaging materials are of special interest as they represent the primary sector within polymer manufacturing [15]. Modern packaging often employs multilayer structures to achieve high performance in terms of toughness, thermal resistance, and barrier properties [24]. The majority of current multilayer structures combine metals and polymers of different chemical constitution in order to ensure good performance.

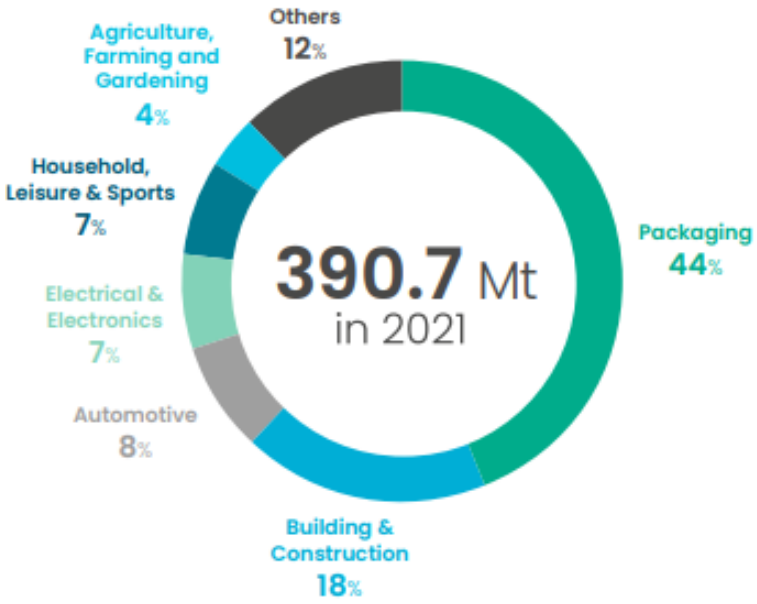


Figure 1.1: Distribution of the global plastic use by application.[1]

This has raised interest in sustainable "monomaterials" alternatives [25, 26]. These systems utilize single or multi-layered builds-ups of polymers with compatible chemical structures, enabling recyclability even when blended. It is not requisite in the use of the "monomaterials" to refer to the same molecular structure, but rather chemical similarity sufficient for reprocessing. Such monomaterial film's behavior is extremely sensitive to morphological structure control at the processing stage.

Macroscopic characteristics of semicrystalline polymer films are controlled by the morphology of their crystalline and amorphous phases, i.e., size, shape, orientation, and connectivity [4, 2, 27, 28]. Manufacturing processes such as Machine Direction Orientation (MDO)–a roller-based process for uniaxial stretching of films–generate mechanical flow aligning polymer chains and hence modifying the "interior" structure of the material [29, 30]. The alignment enhances properties such as elastic modulus, tensile strength, and thermal resistance.

Empirically effective but not yet well understood mechanistically is the connection between process variables such as strain rate and heat gradients and morphological evolution [2, 27, 28, 31, 32]. For example, small changes in cooling rates during MDO can compromise crystalline integrity. Similarly, non-uniform flow fields can result in inhomogeneous crystallite distributions, which will compromise barrier performance. Such uncertainties impede the systematic development of recyclable monomaterials–either single polymer or chemically compatible multilayer materials–intended to replace conventional nonrecyclable composites.

1.4 Morphology of Semicrystalline Polymers

Semicrystalline polymers consist of both crystalline and amorphous regions in their solid state. Unlike relatively "simple" crystalline substances such as metals or ceramics, which have uniform structures, semicrystalline polymers have a complex, hierarchical structure with multiple levels of ordering [4, 10, 2]. This particular morphology results in a number of their physical properties and differentiates them from fully amorphous polymers or crystalline inorganic materials.

1.4.1 Microscopic Structure: Lamellae and Tie Molecules

At their most fundamental level, semicrystalline polymers consist of thin, plate-like crystalline lamellae (ordered polymer regions) that are dispersed in amorphous layers. Each lamellar crystal is a highly ordered region, and between these lamellae lie disordered chains forming an amorphous phase. Although the lamellae are separated by amorphous material, they are not discrete; instead, they are tightly bound by polymer chains crossing the crystal-amorphous boundary. Many polymer chains leave one lamella, pass through the amorphous layer, and enter a neighboring lamella. These connecting chains are commonly referred to as tie molecules, because they effectively link neighboring lamellae together by snapping the amorphous regions[2, 33].

It is important to state that polymer chain folding within lamellae is not perfectly regular, and this creates a significant number of chains extending out of the crystalline regions. Instead of every chain staying within a single crystal, many chain segments exit the lamella and enter the amorphous layer as loops, loose chain ends, or tie molecules before possibly re-entering another crystalline lamella [4, 33]. This imperfect packing (influenced by factors like undercooling during solidification) leads to a network of molecular connections between crystals. All these interlinking chains that cross the crystal-amorphous boundaries form an intimate and strong covalent bond between the crystalline lamellae and the neighboring amorphous material. In essence, the amorphous phase, reinforced by tie molecules, acts as a molecular cement holding together crystalline plates.

1.4.2 Spherulitic Superstructure

On a larger scale, the lamellar crystals in semicrystalline polymers are typically organized into higher-order structures. Crystalline lamellae often form stacks, which will, in turn, be part of still bigger aggregates [34]. After the amorphous phase crystallizes, a common outcome is the formation of spherulites, which are roughly spherical, polycrystalline structures. In a spherulitic morphology, bundles of ribbon-shaped lamellae extend radially outward from a central nucleation point, creating a sphere-like aggregate of crystalline and amorphous material [3]. Spherulites can range in size from micrometers to millimeters, and they are readily observed using polarized light microscopy.

This multi-level hierarchical structure, originating from molecular chain fold organization and

extending to lamellae and tie molecules at the nanoscale, up through lamellar stacks, and finally to spherulitic superstructures at the microscale, dictates the morphology of semicrystalline polymers. In turn, deformation and overall properties of semi-crystalline polymers are strongly dependent on their morphology because of this hierarchical structure. The crystalline and the amorphous phases are closely coupled and must deform together; therefore, any imposed external stress is accommodated by a combination of crystal deformation and extension of the amorphous phase. Consequently, the mechanical behavior under load occurs in multiple stages and modes, such as tie molecule stretching, bending, or slipping of lamella, rather than as one deformation mechanism.

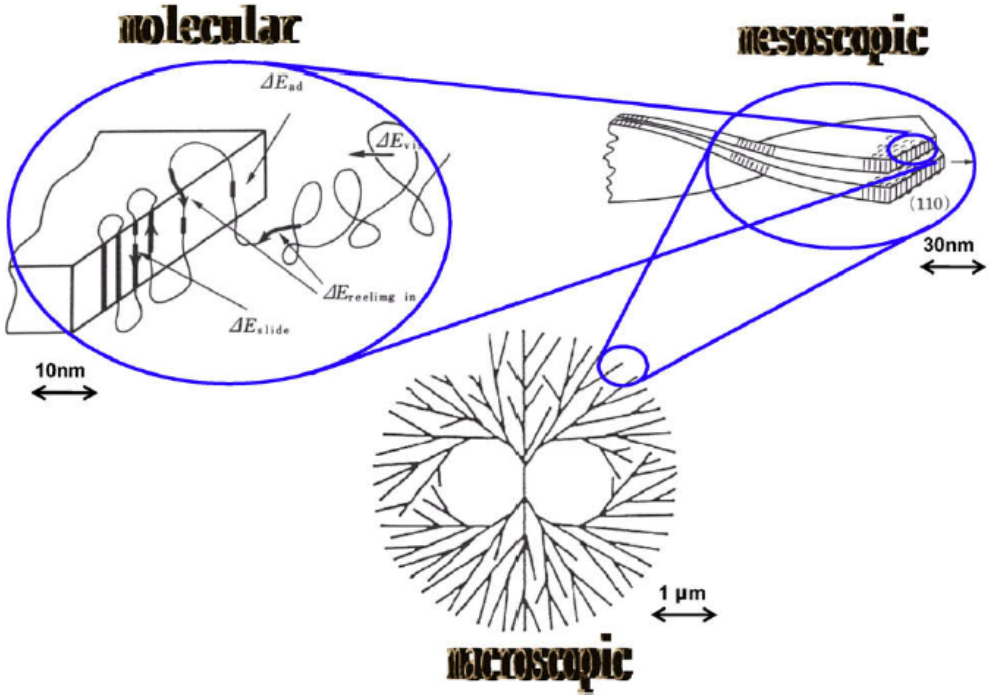


Figure 1.2: Hierarchical structure of semicrystalline polymers illustrating chain folds, lamellae, and spherulitic formations.[2]

1.5 Polymer Crystallization

Regarding the domain of semicrystalline polymers, morphological characteristics are not primarily defined by the design and chemical behavior of the polymer, but rather by modifications that occur during processing. [3]. Temperature, being a significant factor, and pressure, to a lesser degree, are carefully balanced to control and steer the crystallization process effectively. This handle may be a key thermodynamic stage move, requiring the temperature to be controlled below the melting temperature T_m of the polymer, in order to initiate a phase change.

If the temperature is held below T_m, then the crystalline phase's free energy is lower than the free energy of the melt state, driving the system toward crystallization to minimize the overall free energy. In all respects, preserving a temperature below T_m is fairly essential

prerequisite which does not ensure crystallization. Especially in polymers, kinetic barriers may significantly hinder or even prevent the development of the crystal phase. This is often observed below the polymer's glass transition temperature, T_g, where thermal motion is so limited that crystallization becomes impossible. Thus, effective crystallization in polymers takes place in a narrow window of temperature $T_g < T < T_m$ [10, 4, 2, 33].

The crystallization process itself consists of two essential forms: Nucleation and Crystal growth [10, 4, 33]. Nucleation begins with the local organization of polymer chains into a critically sized nucleus. When such nuclei do not grow to a critical size, they dissolve or become remelted. Several factors impact the formation and size of these critical nuclei, the temperature being most significant among them. Lower temperatures promote nucleation by lowering the free energy barrier necessary in forming a stable nucleus.

Subsequent to nucleation, crystal growth proceeds irreversibly when a nucleus reaches critical size. In densely packed polymer systems, crystal segments bond to this nucleus and then grow to replicate across the crystal-amorphous boundary into the surrounding untransformed material[2, 28]. As opposed to nucleation, lowering the temperature adversely impacts the rate of crystal formation, because of the reduced mobility and reduced rearrangement of the polymer chains. Thus, the overall rate of crystallization pivots on a delicate balance between the rates of nucleation and consequent crystal growth.

All in all, the morphology of semi-crystalline polymers is characterized by the interplay between these two processes. Larger spherulites, for example, develop where nucleation rates are low. By controlling crystal growth and nucleation rates, researchers can adjust the size distribution of spherulites and other morphological features to provide desired material properties and performance.

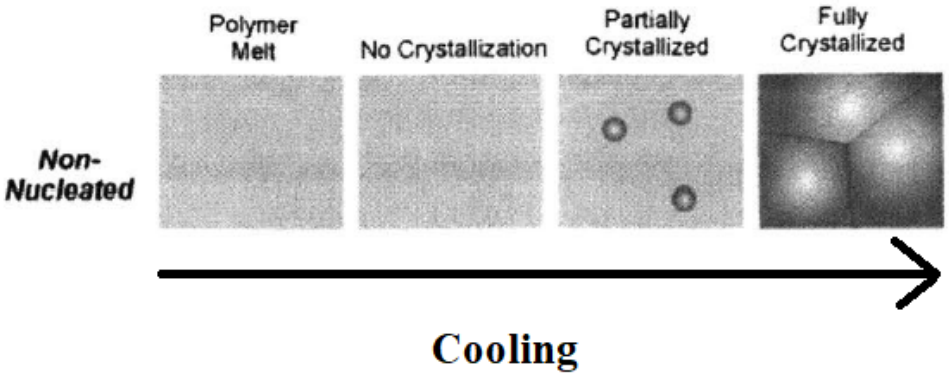


Figure 1.3: Stages of crystallization in polymers, showing the transition from a homogeneous polymer melt (left) to a fully crystallized structure (right).[3]

1.6 Thesis Objective

Crystallization in polymers proceeds through two sequential stages: the formation of initial ordered clusters (nucleation) followed by the subsequent expansion of those clusters into crystalline domains (growth). However, the nucleation phase–particularly homogeneous nucleation in a quiescent (additive free, no flow) melt–remains comparatively less understood and more elusive than the crystal growth phase [35, 36, 37]. Nucleation plays a pivotal role in controlling crystallization, it is often the rate-determining step of the process, since rapid crystal growth can only commence after a stable nucleus has formed. Consequently, the conditions under which nuclei form (e.g. degree of subcooling) largely dictate the overall kinetics and even influence the size, number, and morphology of the resulting crystals. In essence, a deeper understanding of the nucleation step is crucial because it sets the stage for all subsequent crystal growth.

Studying homogeneous crystal nucleation at the molecular level is challenging but greatly aided by computer simulations [38, 39]. Nucleation events occur on a very small length scale (nanometer-sized clusters), which is exceptionally difficult to observe in real-time experiments, yet is well within the spatial capabilities of molecular dynamics (MD) simulations. At the same time, nucleation is a rare, stochastic event that typically unfolds on long timescales (often far beyond the reach of conventional MD runs). To tackle this disparity, one can employ rapid quenching (deep subcooling) in simulations to increase the likelihood of observing nuclei, as extremely high subcooling favors homogeneous nucleation over the more common heterogeneous mode [4]. While practical polymer processing often exploits external forces influences–such as nucleating agents or flow-induced orientation–to stimulate faster nucleation, our focus here is on the fundamental, uninfluenced case of homogeneous nucleation. This "baseline" scenario is of primary importance because most theoretical models of polymer crystallization assume homogeneous nucleation as a starting point, and improved insight into it is necessary for understanding more complex cases with flow or impurities. Accordingly, this thesis employs MD simulations to investigate homogeneous crystal nucleation in a subcooled, quiescent melt of polydisperse polyethylene (PE) chains under rapid quenching and stretching conditions. Through this approach, we aim to elucidate the critical nucleus stage of polymer crystallization, which in turn governs how and how fast subsequent crystal growth unfolds.

Chapter 2

Fundamentals of Homogeneous Crystal Nucleation

2.1 Introduction to PE crystallization

Polyethylene (PE) is a widely used semicrystalline polymer, the crystallization of which has been intensively studied for both fundamental understanding and industrial applications [4]. When a polymer melt crystallizes, it proceeds through two main stages. Nucleation is the early formation of tiny, nascent crystalline regions (nuclei) in the supercooled melt, while growth is the enlargement of these nuclei into larger crystalline regions. In polymer crystallization, nucleation often plays the dominant role in determining the final morphology and properties of the material. This is due to the fact that the number and the spatial distribution of nuclei pave the way to the number of crystalline entities (e.g., spherulites) formed, which in turn influences crystal size, arrangement, and the degree of crystallinity in the solid. It should be pointed out that nucleation is typically the rate-determining step: a significant induction period (a delay before crystals are observed) is controlled by the slow emergence of stable nuclei, whereas once nuclei are formed, subsequent growth of crystals can occur relatively rapidly [4]. Thus, the structure and properties of PE (and other semicrystalline polymers) are strongly influenced by nucleation pathways, often more so than by the process of growth of the crystal itself.

Polymer crystallization can be realized in two ways: heterogeneous nucleation, which takes place on impurities or added nucleating agents, and homogeneous nucleation, which occurs spontaneously in the bulk polymer melt without any foreign surfaces [4]. In practice, most bulk PE crystallizations are initiated heterogeneously at relatively low supercoolings (low undercooling below the melting point) because trace impurities or intentionally added nucleating agents provide favorable sites for crystal initiation [4]. Homogeneous nucleation of

PE is elusive and, therefore, deep supercooling is required (namely ultra-purified melts, tiny droplets, or ultra-fast cooling) to overcome the substantial free energy barrier of nucleus formation [40]. It is a fact that for many years, homogeneous nucleation in polymers was thought to be practically unobservable, however, advances in fast scanning calorimetry and other techniques have shown that it can occur at sufficiently low temperatures (often near or below the glass transition) [40]. In all events, the early nucleation stage influences at a significant level the crystallization kinetics and final crystalline texture.

Recent studies have shifted emphasis on the fact that the initiation of the polymer crystal is a unique phenomenon, not just a miniature version of growth. For instance, molecular simulations of entangled PE melts show that the emergence of a stable nucleus seems to be distinct from crystal growth, involving different molecular ordering processes [41]. In other words, forming the very first ordered cluster (nucleus) from a disordered melt is a separate step with its own kinetics and thermodynamics, rather than a simple continuation of the crystal growth process. This perspective underscores why understanding nucleation is critical: controlling the nucleation stage (e.g., via temperature profiles) provides leverage over the entire crystallization outcome.

Evidence provided during experiments further highlights the dominant role of nucleation in PE crystallization. Time-resolved small-angle X-ray scattering (SAXS) and optical studies have shown that the induction period before observable crystallization corresponds to the nucleation process rather than phase separation phenomena. In a SAXS study on PE containing a nucleating agent, the SAXS intensity remained low for a time (induction time) and then increased sharply as nuclei formed; this induction time shortened dramatically at higher supercoolings, indicating faster nucleation, which proves the dependence of induction time on supercooling, clearly demonstrating that nucleation controls the early stage of PE crystallization [42]. Once nuclei become stable and numerous, crystal growth proceeds, consuming the remaining amorphous material. Hence, from both theoretical and practical standpoints, nucleation is the pivotal step in PE crystallization, often determining the crystallization rate and the resulting semicrystalline structure.

2.2 Nucleation Theories

2.2.1 Classical Nucleation Theory (CNT)

Classical Nucleation theory (CNT) [43] has served as a foundational framework for understanding homogeneous nucleation processes. Initially conceptualized through the pioneering work of Gibbs [44], Volmer and Weber [45], and later expanded by Becker and Döring [46], and Zeldovich [47], the theory was developed to describe phase transitions in systems such as vapor condensation into liquid. Subsequently, these principles were generalized to model crystal nucleation in polymeric melts and solutions [48].

In CNT, the formation of a small crystallite (nucleus) from the melt is treated as a thermally

activated process that balances two competing contributions to the free energy of formation (ΔG) of the system. On one hand, the new crystalline phase is energetically favored by the release of latent heat (or decrease in free energy) in the bulk of the nucleus (a volume free energy term). On the other hand, creating a nucleus introduces an interface between the crystal and melt, incurring an energetic penalty proportional to the surface area (a surface free energy term) [38]. For a nucleus of radius r (assuming, for simplicity, a spherical shape in classical theory), the total free energy change can be expressed qualitatively as,

$$\Delta G(r) = 4\pi r^2 \sigma - \frac{4}{3}\pi r^3 \Delta G_v \tag{2.1}$$

where σ is the crystal-liquid interfacial free energy per unit area and ΔG_v is the Gibbs free energy difference per unit volume between the liquid and crystal phase at the undercooling temperature. At very small r, the surface penalty dominates, so adding molecules to the embryo increases (ΔG); at large r, the volume term dominates, making growth favorable. Figure 2.1. illustrates the typical behavior of (ΔG) as a function of nucleus size: (ΔG) rises to a maximum at a certain critical nucleus size r^* and then decreases for larger nuclei.

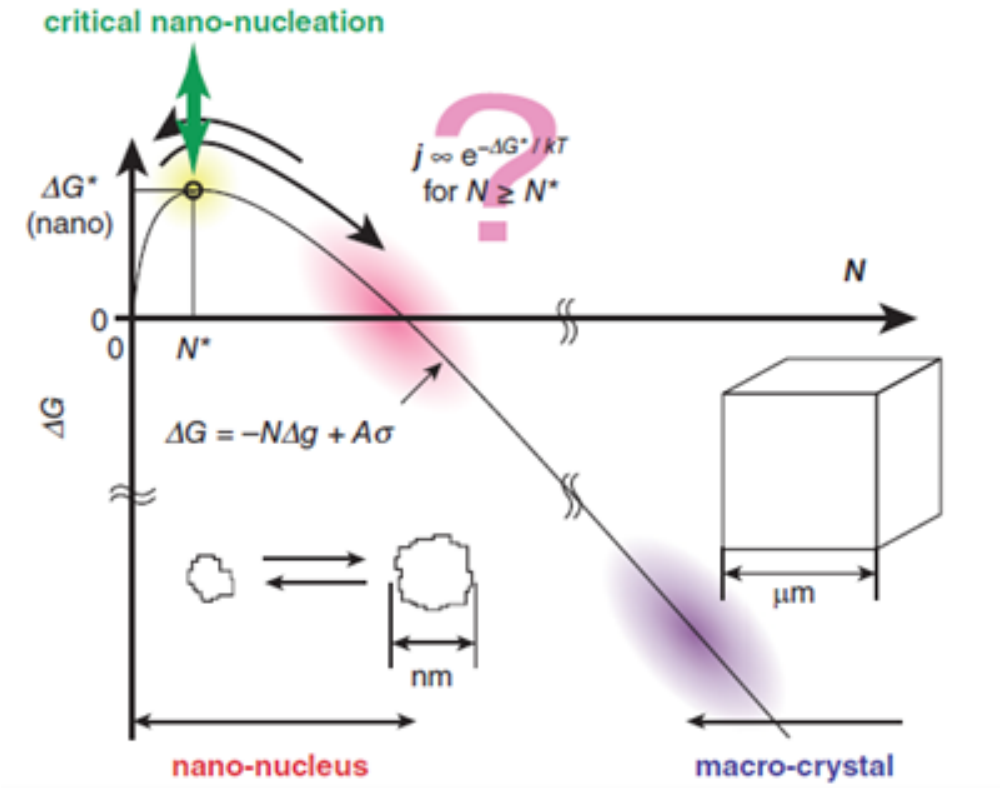


Figure 2.1: Illustration of ΔG versus N, where A represents the surface area of the nucleus. There are notable variations in the size and shape of the nano-nucleus. Δg is associated with critical nano-nucleation, which serves as the activation barrier.[4]

The critical nucleus represents an unstable equilibrium point–an embryo of that size has the

highest free energy barrier to overcome. If thermal fluctuations produce an embryo smaller than critical, it will likely dissolve back in the melt phase (because shrinking lowers the free energy); if an embryo reaches the critical size, it has an opportunity to grow further, since adding more molecules beyond this point will reduce the free energy. The top of the free energy barrier corresponds to the critical nucleus with radius r^*, and the critical free energy (ΔG^*) is the free energy of formation for the critical nucleus.(ΔG^*) and r^* are obtained by maximizing (ΔG) with respect to r in Eq.(2.1) [38],

$$\Delta G^* = \Delta G(r^*) = \frac{16\pi}{3} \cdot \frac{\sigma^3}{(\Delta G_v)^2} \tag{2.2}$$

and

$$r^* = \frac{2\sigma}{\Delta G_v} \tag{2.3}$$

The height of the free energy barrier (ΔG^*) (at $r = r^*$) governs the nucleation rate. Mathematically, CNT often gives an expression for the nucleation rate I (nuclei per volume per time) of the form,

$$I = K \exp\left(-\frac{\Delta G^*}{k_B T}\right) \tag{2.4}$$

where ΔG^* is the Gibbs free energy barrier for forming the critical nucleus, T is temperature, k_B is Boltzmann's constant, and K is a kinetic prefactor that accounts for molecular attachment kinetics and vibration frequencies, often related to an attempt frequency and the Zeldovich (Z) factor in Classical Nucleation Theory (CNT). For polymer melts, an analogous expression is used, although determining ΔG^* and K is nontrivial due to the complexities of polymer chain configurations.

In applying CNT to polymer crystallization, a few modifications are typically made to account for polymer specifics. One classical approach is the Hoffman-Lauritzen theory which treats polymer nuclei as thin crystalline platelets (lamellae) with a folded-chain configuration. In such models, the nucleus is often assumed to have a disk-like shape: a thin lamella with a certain thickness and lateral dimensions. Two types of surface free energies are then considered–one for the basal (folded) surfaces of the lamella and one for the lateral surfaces (chain edges) [38, 49]. The thermodynamics becomes more complex, but the essence is similar: a critical size (thickness and lateral width) exists, balancing the reduced bulk free energy and the increased surface energies.

2.2.2 Limitations of CNT for Polymers

Despite its widespread use, classical nucleation theory has been found to be limited for polymers like PE. CNT assumes that nuclei have the same properties (crystal structure, density,

surface energy) as the bulk crystalline phase and typically considers a simple, idealized shape (spherical or cylindrical). However, nascent polymer nuclei are not so ideal. Recent MD simulations have revealed that nascent polymer crystal nuclei are highly anisotropic and irregular in shape, rather than the near spheres or discs assumed by CNT [50]. In fact, high-symmetry shapes (spheres, cylinders) were found to be thermodynamically unfavorable for small polymer nuclei; instead, the nuclei fluctuate in shape, often have a diffuse, non-uniform interface with the melt [50]. This undermines one of the core assumptions of CNT–a well defined surface energy for a well defined small crystal–and can lead to quantitative discrepancies. For example, using oversimplified geometry and bulk-phase surface energies in CNT can cause orders-of-magnitude errors in predicted nucleation rates for polymers [50]. In PE, a critical nucleus might contain on the order of 100-1000 methylene units, but those units are not arranged in a perfect, smooth-edged crystallite; instead, the nucleus may contain looped, entangled chain segments and a distribution of stem lengths within it [41]. Such internal disorder and variations are not captured by classical theory.

Classical theory also presumes a one-step process–the nucleus forms or does not form, in a single thermodynamic step. There is growing evidence that polymer nucleation may proceed via multi-step pathways, which CNT, in its most basic form, does not consider. For instance, a two-step nucleation mechanism has been proposed for flexible polymers like PE, whereby an initially transient, metastable "pre-ordered" cluster of chains is created, which then reorganizes into a true crystalline nucleus [51]. In this scenario, an intermediate step lowers the free energy barrier by relaxing the entropic penalty before final crystal nucleation. Such intermediate states are beyond the scope of CNT, which would view nucleation as the direct appearance of the crystalline phase from the melt.

All in all, CNT provided the basic language (critical nucleus, free energy barrier) and qualitatively predicts trend (e.g., higher supercooling lowers the barrier and accelerates nucleation). Thus, CNT remains a starting point for the understanding of nucleation, and the majority of polymer crystallization studies refer to its concepts as a reference.

2.2.3 Density Functional Theory (DFT)

One of the most powerful criticisms of CNT is the capillary approximation, i.e., small portions of the new phase are treated as though they are macroscopic regions in space, and that material at the center of nucleus behaves like the new phase in bulk; and that surface free energy of a small cluster is the same as that of an infinite planar surface. These approximations can only be deemphasized if the nuclei are sufficiently large, and CNT is therefore best for nucleation near equilibrium coexistence. Far away from the coexistence, especially in regions of spinodal decomposition, CNT could become very inaccurate; as a matter of fact, the experimentally determined and CNT predicted nucleation rates based on independently determined thermodynamics quantities such as interfacial free energies and heat of fusion tend to be orders of magnitude different. In such cases, more sophisticated theory is needed.

At the heart of DFT is the concept of a free energy functional. Instead of characterizing the nucleus by a single size or volume, DFT treats the free energy ΔG as a functional of the spatial density distribution $\rho(\mathbf{r})$. This means ΔG depends on the entire density profile throughout space. The stable or critical configurations of the system are those density profiles that (locally) extremize this functional (i.e., minimize the free energy under appropriate constraints).

A brief review of the available literature reveals that, for gas-liquid nucleation, DFT has solved issues for weakly polar liquids and has given rise to explanations of the dynamics of the behavior of nonpolar fluids [52]. For binary condensation, researchers have formulated the nucleation theorem, a relationship between the effect of pressure, or chemical potential, on the free energy of the critical nucleus size and its size and composition [53]. Lastly, research groups that began with the gas-liquid nucleation, extended the DFT method to the solid-liquid transition, applying it in metal alloy crystallization. They observed that the properties of a critical nucleus size can differ significantly from those of the stable bulk phase that eventually forms [54].

2.3 Experimental Studies on PE Nucleation

Experimentally investigating nucleation in polyethylene is challenging because nuclei are nanoscopic and form rapidly during supercooling. However, over the years, researchers have developed techniques to infer nucleation behavior by measuring indirect observables (like heat flow, optical signals, or scattering) that are sensitive to the early stages of crystallization. Key experimental approaches include differential scanning calorimetry for thermal analysis, optical microscopy for direct observation of crystallites, and X-ray scattering for probing nanoscale structure formation. Each method provides insights into nucleation rates, induction times, and the effects of additives (nucleating agents) on the nucleation process.

2.3.1 Differential Scanning Calorimetry (DSC)

DSC is one of the most widely exploited methods to study polymer crystallization, including that of PE [33]. In a DSC measurement, the polymer sample is cooled down from the melt (or heated), and the heat flow is measured. The exothermic release of the latent heat during crystallization produces a peak in the DSC thermograph. From isothermal or non-isothermal DSC data, one can extract the onset time of crystallization (which correlates with the nucleation induction time) and the overall rate of heat evolution (related to the combined effect of nucleation and growth). For example, in isothermal crystallization experiments, a longer induction time before the exotherm indicates slower nucleation at that temperature. By analyzing how induction time or crystallization half-time varies with temperature (supercooling), nucleation kinetics can be extrapolated. Standard DSC, nevertheless, averages over the whole sample and does not resolve the very first nuclei directly. It typically detects crystallization once a significant fraction of material has crystallized (when growth is also

initiated).

Advancements like modulated-temperature DSC (MT-DSC) and fast scanning calorimetry (FSC) have improved our ability to study nucleation. MT-DSC imposes an extremely small oscillatory temperature modulation on the linear cooling ramp, yielding separation of reversing (heat-capacity related) and non-reversing (kinetic, crystallization-related) heat flows [33]. This can help identify weak thermal events such as the early stages of nucleation that might be masked in standard DSC. Fast scanning calorimetry, on the other hand, achieves extremely high cooling and heating rates, ranging from 10^3 to 10^6 K/s, which makes it possible to bypass rapid crystallization and trap polymer melts in deeply supercooled states [40]. Using FSC, researchers have been able to observe homogeneous nucleation in polymers by cooling so fast that heterogeneous nucleation is suppressed; then by reheating at various rates, they probe the "stored" nuclei formed homogeneously at low temperature. For instance, Schick et al. reported that PE and other polymers exhibit measurable homogeneous nucleation when cooled near the glass transition temperature, with a nucleation rate that peaks around that temperature in accordance with CNT expectations [40]. This calorimetric techniques provide quantitative data on nucleation rates and energy barriers when interpreted through theoretical models.

2.3.2 Polarizing Optical Microscopy (POM)

Polarizing optical microscopy is a powerful visual tool to study spherulitic crystallization in polymers. Under crossed polarizers, semicrystalline polymers like PE exhibit birefringence; as spherulites grow, they appear as bright maltese-cross patterns against a dark background. By observing a quiescent melt of PE as it is crystallized isothermally, one can directly count the number of spherulites that nucleate and measure the time at which each becomes visible. This provides direct information on the nucleation rate (especially the heterogeneous nucleation rate, since each spherulite typically originates from a nucleation site). For example, one can perform an isothermal crystallization at a certain temperature and count the number of spherulites per unit volume that appear over time–the slope of that curve at early times is the nucleation rate I. In practice, at a fixed supercooling, the number of nuclei often increases linearly after an initial induction period, consistent with a roughly constant steady-state nucleation rate [42]. POM can also distinguish between instantaneous nucleation (all nuclei appearing at once, yielding many small spherulites) versus sporadic nucleation (nuclei appearing continuously over time, yielding a distribution of spherulite sizes). In polyethylene, typically a continuous (sporadic) nucleation is observed over the crystallization period, especially if the melt contains some impurities which activate at different times or if some fraction of nuclei form slightly later.

Through POM, one can also assess the influence of nucleating agents. A nucleating agent (NA) is an additive–often a particulate filler or a specific chemical compound–that provides surfaces which lower the free energy barrier for nucleation (thereby promoting heterogeneous nucleation). In PE, common nucleating agents include certain inorganic particles or organic

compounds that have some epitaxial match with the PE crystal lattice. When such an NA is present, POM typically shows a dramatically increased number of spherulites (nuclei) and a reduced induction time. SAXS studies on PE with a nucleating agent found that the initial SAXS intensity (which is proportional to the concentration of very small nuclei or density fluctuations) was enhanced by orders of magnitude [42]. In one case, adding $\sim 3\,\mathrm{wt}\%$ of a nucleating agent to PE increased the SAXS signal from nuclei by a factor of 10^4, effectively making otherwise undetectable "nano-nuclei" observable. Correspondingly, POM images of nucleated PE would show a fine grain structure with a high density of tiny spherulites, reflecting that high nucleation rate. Nucleating agents not only speed up crystallization (shorter induction period and overall crystallization time) but also can improve material properties by refining the microstructure (for example, smaller, more uniform spherulites can enhance clarity or toughness in plastics).

2.3.3 Synchrotron X-ray Scattering (SAXS/WAXS)

X-ray scattering techniques, especially with intense synchrotron sources, have proven invaluable for probing early-stage polymer crystallization. Small-angle X-ray scattering (SAXS) is sensitive to nanoscale density fluctuations and can detect the formation of nanoscopic crystalline clusters (nuclei) before they grow large enough to be seen by optical methods. In nucleation studies, time-resolved SAXS is often performed during isothermal crystallization: one monitors the SAXS intensity $I_X(q,t)$ as a function of time at a given scattering vector q (related to a length scale of a few to tens of nanometers) [4]. An increase in SAXS intensity at small q indicates the appearance of new density heterogeneities on the corresponding length scale–which, in a crystallizing polymer melt, the formation of lamellar stacks once they reach a certain size/thickness. By carefully analyzing the SAXS intensity and its Guinier regime, researchers can estimate the radius of gyration of the growing nuclei and even obtain the size distribution of nuclei as a function of time [4].

One illuminating SAXS experiment on PE (as mentioned earlier) involved doping the polymer with nucleating agent to boost the SAXS signal from nuclei [42]. During isothermal crystallization at a moderate supercooling (around 10-13 K undercooling), the SAXS intensity was observed to increase slowly after a short delay, reflecting the gradual appearance of nuclei. At higher supercooling, the rate of increase of SAXS intensity was much faster, consistent with a higher nucleation rate. By analyzing the q-dependence of the scattering, that study could determine not only the number density of nuclei but also their approximate shape (which was found to be disk-like, consistent with nascent lamellae). SAXS thus directly confirmed that what was changing during the induction period was the formation of nano-nuclei, not some other form of density fluctuation like spinodal decomposition [4, 42]. This kind of direct observation is extremely valuable, as it backs out kinetic parameters for nucleation. For example, from the induction time vs temperature data, one can extract nucleation activation energies or estimate surface free energies by fitting to CNT-based models.

Wide-angle X-ray scattering (WAXS) and electron diffraction are complementary techniques that detect the crystallographic structure once crystals have formed. WAXS can confirm that the nuclei detected by SAXS are indeed PE crystals by the appearance of Bragg peaks corresponding to PE's orthorhombic unit cell. In early stages, WAXS may show very broad (low intensity) crystal peaks, indicating tiny crystallites. The time at which WAXS peaks emerge can be compared to SAXS and DSC to build a consistent picture of when nuclei become "crystalline" enough to diffract and how fast they grow.

Other experimental techniques have also contributed to understanding nucleation in PE. For instance, time-resolved infrared spectroscopy (FTIR) can monitor conformational ordering (appearance of trans conformers) before crystals are large enough to scatter strongly, potentially catching the "pre-ordering" preceding nucleation [51]. Light scattering (small-angle light scattering) can sometimes detect early density fluctuations in transparent polymers. Rheological measurements can indirectly sense crystallization–the melt viscosity or modulus begins to change when crystallites (even very small ones) start to form, thus providing a kinetic trace of nucleation and growth.

2.4 Computational Studies of PE Nucleation

2.4.1 Molecular Dynamics (MD) Simulations

MD involves numerically integrating the equations of motion for a collection of interacting atoms or beads, allowing one to watch how a polymer melt evolves in time at the atomic level. For polyethylene, both atomistic MD (often using a united-atom force field where each $-CH_2-$ is one interaction site) and coarse-grained MD (where several CH_2 units might be lumped into a single bead) have been employed. MD simulations of homogeneous nucleation are extremely demanding, because nucleation is a rare event–the simulation must capture a spontaneous fluctuation of a handful of chains into an ordered nucleus. To observe this in a straightforward MD, one often has to supercool the system significantly (to speed up nucleation) and use a small system volume (to reduce the number of atoms), which can bias the outcome. Despite these challenges, notable successes have been achieved. For instance, early large-scale MD simulations by researchers like Yi and Rutledge managed to observe homogeneous crystal nucleation in a supercooled polyethylene melt [55]. In one such study, the critical nucleus was estimated to contain on the order of $\sim$ 150 carbons at a supercooling of about 30% of the melting temperature. These simulations confirmed qualitatively the existence of a free energy barrier and critical nucleus size, but also revealed the irregular nature of the nuclei.

Modern MD studies, often leveraging parallel computing, have pushed further. Hall and coworkers, for example, performed MD simulations tracking millions of individuals crystalline clusters forming in entangled PE melts to statistically analyze nucleus shapes and sizes [50]. They found that incipient nuclei tend to be irregularly shaped and anisotropic, lacking the symmetry that earlier models assumed. By analyzing a huge number of nucleation

events, they could extract distributions of clusters geometries and detect the necessity of post-critical rearrangements for those clusters to evolve into stable lamellae [50]. Another group (Luo and Sommer) used coarse-grained MD to examine how entanglements influence nucleation, by simulating a polymer (poly(vinyl alcohol)) melt with varying chain lengths [56, 57]. They observed that a high entanglement density can inhibit or delay nucleation, because the molecular mobility needed to form an ordered nucleus is impeded when chains are topologically constrained. This finding, sometimes phrased as "frozen topology" effects, aligns with the idea that polymer nucleation is not just thermodynamics but also strongly kinetics-controlled by chain dynamics. Entangled chains need to pull out of each other's way to align and fold into a crystal, which can be much slower than the corresponding process in a low molecular weight system.

To overcome timescale limitations, MD researchers have also employed strategies like biased or accelerated MD. Examples include the use of umbrella sampling or forward flux sampling to specifically target the nucleation event. In these methods, an order parameter (such as the size of the largest crystalline cluster) is defined, and the simulation is guided or reweighted to sample the rare transition over the nucleation barrier. Tang et al took such an approach to calculate the free energy landscape of polymer nucleation [58, 59]. By doing so, they could estimate the critical nucleus size and nucleation barrier for entangled systems and examine how it depends (or doesn't depend) on polymer molecular weight. Interestingly, their results indicated that beyond a certain chain length (beyond the entanglement length), the critical nucleus size and barrier height were almost independent of molecular weight. This suggests that once chains are long enough to be well-entangled, adding more length (and thus more entanglements) doesn't further slow nucleation excessively. This insight bridges to experimental observations that very high molecular weight PE does not necessarily crystallize much more slowly than moderately high molecular weight PE when both are well entangled.

2.4.2 Monte Carlo (MC)

Monte Carlo simulation provided an alternative approach to sampling polymer configurations and nucleation events by random moves and statistical weights rather than deterministic dynamics. A variety of MC approaches have been used to study polymer crystallization. For example, Hu and co-workers used the kinetic Monte Carlo lattice method to study the growth of polymer crystals and could access other dynamic regimes [60, 61, 62, 63]. Moreover, Karayiannis and co-workers [64, 65] have studied the crystallization of freely jointed hard sphere polymers with an off-lattice kinetic Monte Carlo approach.

All in all, these models, although simplified, can access longer timescales and larger system sizes than atomistic MD, making it possible to observe nucleation and growth of multiple crystallites.

2.4.3 Key Insights from Simulations

Computational studies have significantly extended our understanding beyond what classical theory and experiments alone tell us. A recurring insight is the confirmation of multi-step nucleation behavior in polymers. Molecular simulations of PE have directly shown evidence of an intermediate stage of ordering: a slight local increase in density or orientational alignment of segments can occur before clear crystallinity sets in [51]. This pre-ordering can be seen as a precursor cluster that is not yet fully crystalline (not sharp Bragg peaks in simulation) but has lower mobility and some local structure. Eventually, one part of this cluster might solidify into a tiny crystallite, which then constitutes the nucleus. The simulation by Xu, Tang, and others suggests that this two-step mechanism can expedite nucleation by circumventing some of the entropy barrier–effectively, some ordering happens first (perhaps driven by favorable intrachain arrangements or local density fluctuations), and then the strongly favorable crystal structure emerges within that ordered blob. This nuanced picture goes beyond CNT's one-step assumption and is a major contribution of simulations.

Finally, computational studies have addressed specific conditions such as flow-included nucleation [31, 32]. Under flow (shear or elongation), polymer chain can stretch and align, drastically reducing the nucleation barrier. Nicholson and Rutledge performed MD simulations of n-eicosane (C20, a shorter analog of PE) under shear and uniaxial extension and observed that flow can induce precursors that lead to much faster nucleation [66]. Their results quantitatively show how orientation (a nematic-like ordering) due to flow couples with crystallization–essentially, flow creates oriented clusters that act as effective nuclei. This helps interpret experimental observations in polymer processing where applied stress is known to promote crystallization.

Chapter 3

Fundamentals of Molecular Simulations

In this chapter, we introduce definitions and background knowledge that will form the basis of other concepts and methods presented later in this study. We start our discussion by introducing the formalism of statistical mechanics and briefly describing the statistical ensembles used in computer simulations. Then, the principles of Monte Carlo (MC) & Molecular dynamics (MD) methods are described, with more detail given to the latter. Finally, we conclude by describing the empirical force field used in this thesis to effectively describe the interaction between the molecules.

3.1 Statistical Mechanics and Ensembles

3.1.1 Basics of Statistical Mechanics

A system of N classical particles can be described by its microstate, specified by a point in a $6N$-dimensional phase space comprising all particle coordinates and momenta. We denote a phase-space point as $\Gamma \equiv (\mathbf{q}_i, \mathbf{p}_i)$, with $i = 1, \ldots, N$ labeling particles. As the system evolves under Newton's equations (equivalently Hamilton's equations for conservative forces), $\Gamma(t)$ traces out a trajectory in phase space. Liouville's theorem asserts that the flow of an isolated Hamiltonian system in phase space is incompressible – the phase-space probability density remains constant along trajectories [7, 67]. In other words, if we imagine an ensemble of identical systems started in a small volume of phase space, that "cloud" of phase points will move and deform but maintain the same total volume. This conservation of phase-space volume guarantees that no microstates are gained or lost as an isolated system evolves, providing the foundation for connecting dynamics to statistics. It also implies that if the initial distribution of phase points is the equilibrium one, it will remain invariant in time.

Another key concept is the ergodic hypothesis. Originally proposed by Boltzmann, it posits that over long times, a single system will visit all accessible microstates consistent with the

conserved quantities (e.g. energy) and spend time in each region of phase space in proportion to the region's volume [68]. In practical terms, ergodicity means that time averages along one sufficiently long trajectory equal ensemble averages over a hypothetical collection of systems. For an ergodic system in equilibrium, no region of phase space is permanently inaccessible; given enough time, the system explores the entire energy hypersurface. Ensuring that a simulation algorithm is ergodic is crucial – if the integrator or model restricts the system to a subset of configurations, the results will not reflect the true equilibrium ensemble. In systems like simple fluids at moderate conditions, ergodicity is believed to hold and underpins the validity of using single MD trajectories to compute equilibrium properties [7, 67]. Under the ergodic assumption, any macroscopic observable A can be obtained as a phase-space average over the appropriate probability distribution $\rho(\Gamma)$, which is equal to a long-time average of A in a single experiment or simulation. For example, the ensemble average of A is defined as,

$$\langle A \rangle = \int A(\Gamma)\, \rho(\Gamma)\, d\Gamma \tag{3.1}$$

where $\rho(\Gamma)$ is normalized so that $\int \rho(\Gamma) d\Gamma = 1$. This bridges microscopic states to macroscopic observables: thermodynamic quantities like pressure, energy, and entropy can be expressed as appropriate averages of microscopic functions $A(\Gamma)$ over the equilibrium ensemble. Notably, if ergodicity holds, one can equivalently compute $\langle A \rangle$ by averaging $A(t)$ over a long MD trajectory. This connection between time averages and ensemble averages (Boltzmann's ergodic hypothesis) is what allows Molecular Dynamics to predict equilibrium properties.

In statistical mechanics, a macrostate is defined by a set of thermodynamic control parameters (e.g. (N, V, E) for an isolated system). An ensemble is a large collection of virtual copies of the system, each representing a possible microstate consistent with the given macrostate constraints [7, 67]. Different ensembles correspond to different physical constraints (energy exchange, particle exchange, etc.). For a given ensemble, statistical mechanics postulates that in equilibrium the probability of finding the system in microstate Γ is proportional to $\exp(-\beta H(\Gamma))$ if the system can exchange energy with a heat bath, where $H(\Gamma)$ is the Hamiltonian (total energy) and $\beta = \frac{1}{k_B T}$. More generally, each ensemble has an associated characteristic distribution: for example, in the microcanonical ensemble (fixed E) all accessible states of energy E are equally probable, whereas in the canonical ensemble (fixed T) states are weighted by the Boltzmann factor $e^{-\beta E}$ [7, 67]. The partition function is the normalization factor for these probabilities and encodes the statistical weight of all microstates. In a discrete description, the canonical partition function is,

$$Q(N, V, T) = \sum_i e^{-\beta E_i} \tag{3.2}$$

which sums over all microstates i (with energy E_i) consistent with given N, V, T. This central quantity links microscopic energies to macroscopic thermodynamics; for instance, the Helmholtz free energy is $A = -k_B T \ln Q$ [7, 67]. In continuous phase space, Q includes inte-

grals over coordinates and momenta (with the appropriate $1/(N!h^{3N})$ factor to account for in distinguishability and continuous states). The Boltzmann distribution for the canonical ensemble follows immediately: the probability density of microstate Γ is $\rho_{NVT}(\Gamma) = \frac{1}{Q}e^{-\beta H(\Gamma)}$, which indeed gives $\rho \propto e^{-\beta E}$. This result can be derived by considering a system in weak contact with a large heat bath and using the principle of maximum entropy or by counting the composite microstates of system + bath. The Boltzmann distribution is a cornerstone of statistical mechanics, explaining why higher-energy configurations are exponentially suppressed at low temperature, and it reduces to equal a priori probabilities in the limit of no temperature control (consistent with the microcanonical postulate). The partition function for other ensembles is defined similarly as the normalizing sum or integral of the appropriate Boltzmann factors.

Because thermodynamic observables can be obtained as derivatives of the log of the partition function, ensemble averages provide a direct link from microscopic quantities to macroscopic equations of state. For example, the average internal energy U in the canonical ensemble is $\langle E\rangle = -\partial \ln Q/\partial\beta$, and the specific heat relates to energy fluctuations [7, 67]. Equipartition is another fundamental result: it follows from the quadratic dependence of kinetic energy on momenta that each degree of freedom contributes $\frac{1}{2}k_{\mathrm{B}}T$ to the average kinetic energy at temperature T. Thus, $\langle p^2/(2m)\rangle = \frac{1}{2}k_{\mathrm{B}}T$ for each momentum component, leading to $\langle K\rangle = \frac{3N}{2}k_{\mathrm{B}}T$ for N particles (when only translational kinetic energy is considered). This provides a microscopic interpretation of temperature. Likewise, the virial theorem connects microscopic motion to pressure [7, 67]. In a system with volume V, the pressure P can be obtained from Newton's equations via the virial expression,

$$PV = Nk_{\mathrm{B}}T + \frac{1}{3}\left\langle \sum_{i=1}^{N} \mathbf{r}_i \cdot \mathbf{F}_i \right\rangle \tag{3.3}$$

often written as $P = \frac{Nk_{\mathrm{B}}T}{V} + \frac{1}{3V}\langle \sum_i \mathbf{r}_i \cdot \mathbf{F}_i\rangle$. Here $\mathbf{F}_i$ is the force on particle i, and the sum $\sum \mathbf{r}\cdot\mathbf{F}$ is the virial of the forces. The first term $(Nk_{\mathrm{B}}T)/V$ is the ideal gas contribution (coming from momentum degrees of freedom via equipartition), while the second term accounts for inter-particle interactions (it is negative for attractive forces in liquids, lowering the pressure from the ideal gas value).

In molecular dynamics simulations, one computes pressure using this formula at each time step and then averages it, thus directly connecting the microscopic force calculations to a macroscopic pressure observable. These examples illustrate how statistical mechanics serves as a bridge between microscopic trajectories (positions, momenta, forces) and bulk properties: by identifying the appropriate ensemble for the conditions of interest, we can derive formulas that allow computation of thermodynamic observables from the microscopic behavior.

3.1.2 Ensemble Theory and MD

There are several ensembles of equilibrium statistical mechanics, each used under different experimental conditions. In particular, the primary are the microcanonical (NVE), canonical (NVT), and isothermal–isobaric (NPT). In this subsection, we briefly review each ensemble and its implementation in molecular dynamics (MD) [7].

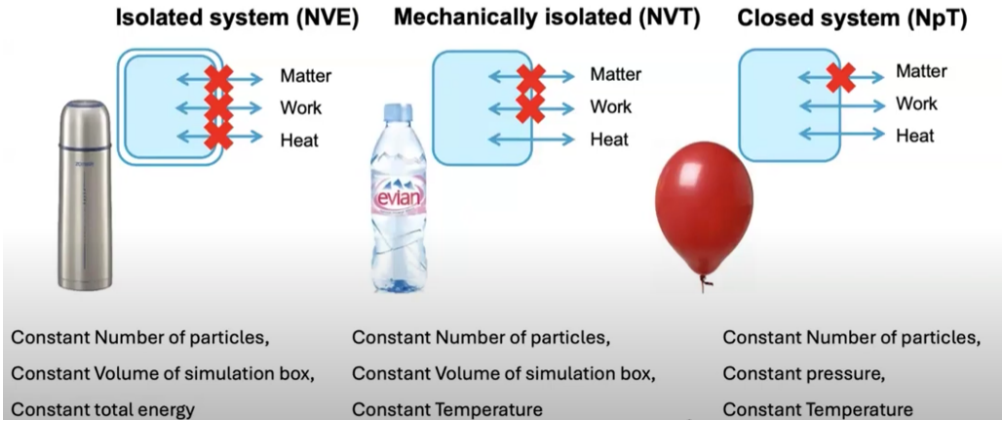


Figure 3.1: Schematic Representation of microcanonical (NVE), canonical (NVT) and isothermal-isobaric (NPT) statistical ensembles [5].

Microcanonical Ensemble (NVE)

This represents an isolated system with fixed number of particles N, fixed volume V, and fixed total energy E. No heat or matter is exchanged with the surroundings. In the microcanonical ensemble, all accessible microstates with the given energy E are equally likely – the probability density is uniform over the hypersurface $H(q, p) = E$ in phase space. The microcanonical partition function (often denoted Ω or Q_{NVE}) essentially counts the number of states with energy E [7]. MD naturally generates an NVE ensemble when one integrates Newton's equations for an isolated system: in an ideal MD with perfectly conservative forces and no coupling to a bath, the total energy is conserved (apart from numerical integration errors). Thus, a straightforward MD integrator (like velocity Verlet with a sufficiently small time step) yields a trajectory in the NVE ensemble, sampling states on a constant-energy surface. In practice, truly isolated conditions are simulated by using periodic boundary conditions (to avoid surface effects) and no thermostat or barostat. One must ensure energy drift is negligible to maintain NVE conditions [69]. NVE simulations are useful for checking energy conservation and studying inherent dynamical properties. However, experimental conditions often impose constant temperature or pressure, so other ensembles are frequently more appropriate for direct comparison to experiment.

Canonical Ensemble (NVT)

This ensemble fixes N and V as before, but allows the system to exchange energy with a heat bath such that the temperature T is maintained constant. The number of particles and

volume remain fixed, but the energy E can fluctuate. Physically, one can imagine the system in a large thermostatting environment at temperature T. The probability distribution for the NVT ensemble is the Boltzmann distribution [7],

$$\rho_{NVT}(\{q,p\}) \propto \exp\left[-\frac{H(\{q,p\})}{k_{\mathrm{B}}T}\right] \tag{3.4}$$

We have already introduced the canonical partition function $Z(N,V,T)$ above. In MD simulations, achieving the NVT ensemble requires introducing a thermostat algorithm that regulates kinetic energy to reach and maintain the desired T.

Deterministic extended-system thermostats

The Nosé–Hoover thermostat is a common method which extends the system's equations of motion by adding a fictitious thermostat variable that interacts with the physical degrees of freedom. This approach produces trajectories that sample the canonical ensemble when averaged over time. Nosé–Hoover thermostats tend to preserve realistic dynamics over long timescales, but can exhibit oscillatory energy exchange or fail to thermalize very stiff modes unless thermostat chains are used. Another extended-system method for NVT is the Martyna–Tobias–Klein (MTK) thermostat (a refinement of Nosé–Hoover with improved stability) [69].

Stochastic thermostats

These thermostats introduce random forces or velocity rescaling to enforce a canonical distribution. The Andersen thermostat randomizes the velocity of a randomly chosen particle at fixed intervals (mimicking collisions with an imaginary bath) to generate a correct NVT ensemble [69].

Velocity-rescaling thermostats

The Berendsen thermostat rescales particle velocities towards the target temperature using a first-order relaxation model. This provides gentle temperature control and is very effective for equilibrating systems. However, Berendsen coupling does not generate the exact canonical ensemble – it suppresses the natural energy fluctuations. As noted in the GROMACS manual, the Berendsen thermostat produces the correct average temperature but not the correct distribution of kinetic energy (the error in sampling decays as $1/N$ for large systems). Thus, it is often used only for initial equilibration. A variant called stochastic velocity rescaling adds a random component to Berendsen's scheme to recover proper canonical fluctuations [69].

Isothermal-Isobaric Ensemble (NPT)

This ensemble keeps N fixed while holding temperature T and pressure P constant. The system can exchange both heat and volume with the environment: imagine the system

in a piston-and-thermostat arrangement where the pressure is imposed externally and the walls can move. In the NPT ensemble, both energy and volume fluctuate. The equilibrium probability density is given by [7],

$$\rho_{NPT}(\{q,p\};V) \propto \exp\left[-\frac{H(\{q,p\})+PV}{k_BT}\right] \tag{3.5}$$

i.e. proportional to $e^{-\beta(E+PV)}$. The corresponding partition function $Q_{NPT}(N,P,T)$ involves an integral over all volumes and an integral over phase space at each volume. The thermodynamic potential associated with NPT is the Gibbs free energy $G(N,P,T) = -k_BT\ln Q_{NPT}$. To realize an NPT ensemble in MD, one must employ both a thermostat (to control T) and a barostat (to control pressure). A barostat dynamically adjusts the simulation box volume to maintain the target pressure on average.

Berendsen barostat

Similar in spirit to the Berendsen thermostat, it rescales the volume (and particle coordinates) towards the target pressure with a specified relaxation time. This produces the correct average pressure but does not rigorously generate the NPT ensemble. It is useful for equilibration, as it damps pressure oscillations quickly, but it underestimates volume fluctuations.

Parrinello–Rahman barostat

An extended ensemble approach introduced by Parrinello and Rahman (1981) that treats the simulation box vectors as dynamical variables with an associated "barostat mass". Essentially, the system's Lagrangian is augmented to include kinetic energy terms for the box degrees of freedom coupled to the internal pressure [69]. This method (and variants like Andersen's barostat or the MTK barostat which is a Nosé–Hoover style formulation for pressure) can sample the NPT ensemble correctly. The Parrinello–Rahman method also allows anisotropic stress/strain fluctuations, enabling simulations of variable box shape (important for studying phase transitions that involve symmetry changes, e.g., crystallization). It can, however, lead to oscillatory box dynamics if the system is far from equilibrium or if the barostat "mass" (coupling constant) is not chosen carefully. It's often combined with Nosé–Hoover thermal coupling (NH-NPT) for rigorous NPT sampling [69].

3.2 Monte Carlo (MC) Method

3.2.1 Principles of Monte Carlo Simulations

The Monte Carlo method occupies a unique place in the history of molecular simulations, since it was the first method employed to perform simulations on a molecular system. Statisticians had been using sampling models to solve mathematical problems since the early 20th century. Nonetheless, this particular method suggested that such problems could be

solved using a probability analogy from a stochastic sampling experiment. The Monte Carlo method, therefore, is a stochastic method that uses a random number generator to search for mathematical and physical answers.

Polymer chains are systems that can acquire an enormous variety of conformations. For various dynamic systems, such as chains, the phase space can be utilized to indicate the possible states they may have. Phase space essentially represents all the possible states a system can assume. Each possible state is represented by one point in this space. Therefore, if there were a way to "explore" these spaces, useful conclusions could be drawn regarding the properties of a system [32].

In their most basic version, MC simulations are carried out by sampling trial moves for the molecules from a uniform distribution. For instance, in a canonical (NVT) ensemble simulation, a randomly selected molecule is displaced, again randomly, to a new position. The trial move is either accepted or rejected based on an importance sampling scheme [67]. The probability of accepting a move, P_{accept}, takes the form

$$P_{\text{accept}} = \min\left[1, \frac{P(\mathcal{O}|\mathcal{N})P(\mathcal{N})}{P(\mathcal{N}|\mathcal{O})P(\mathcal{O})}\right] \tag{3.6}$$

will asymptotically sample the configuration space according to a probability P. In the above equation, P_{accept} is the probability with which trial moves are accepted or rejected, $P(\mathcal{N}|\mathcal{O})$ being the probability for moving from state $\mathcal{O}$ to state $\mathcal{N}$ by performing a trial move, and $P(\mathcal{O})$ being the probability of being at state$\mathcal{O}$. This means that, at equilibrium, the average number of accepted trial moves that result in the system leaving state $\mathcal{O}$ must be exactly equal to the number of accepted trial moves from all other states $\mathcal{N}$ to the state $\mathcal{O}$.

In the original Metropolis scheme, the probabilities $P(\mathcal{N}|\mathcal{O})$ form a symmetric matrix. In this case, there is no bias involved in making the move, and the above equation reduces to the standard Metropolis acceptance criterion

$$P_{\text{accept}} = \min\left\{1, \exp\left[\frac{-\mathcal{V}(\mathcal{N}) - \mathcal{V}(\mathcal{O})}{k_B T}\right]\right\} \tag{3.7}$$

The advanced MC methods are based on judicious choices of $P(\mathcal{N}|\mathcal{O})$. Furthermore, a computational advantage of MC over MD is that only the energy needs to be calculated, not the forces, so (CPU) time per step is less than in an MD simulation.

3.2.2 Monte Carlo-Driven Equilibration for Molecular Dynamics Simulations

Molecular Dynamics (MD) simulations propagate atoms along physically realistic trajectories, which means that relaxing a complex system can require simulating very long real-time scales. For polymer melts with long chains that wind and intertwine, reaching equilibrium through MD alone can demand simulation times on the order of milliseconds or even minutes

of physical time, far beyond what is typically feasible computationally.

One strategy to accelerate MD equilibration is to coarse-grain the polymer model, reducing the level of atomic detail. For example, multiple atoms along a polymer backbone can be grouped into a single bead (a united-atom or pseudo-atom representation, such as treating each $-CH_2-$ or $-CH_3$ group in polyethylene as one interaction site) [7, 67, 6]. This simplification reduces the number of interaction sites and smooths out high-frequency degrees of freedom, allowing larger MD time steps and faster relaxation of the model polymer.

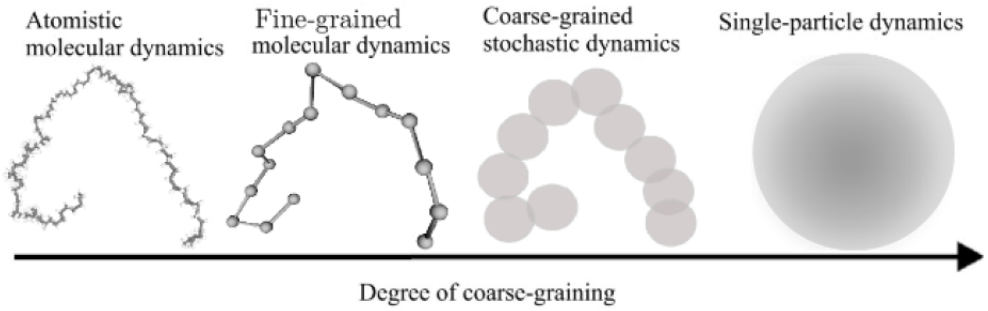


Figure 3.2: Schematic Representation of different levels of coarse-graining [6]

Monte Carlo simulations offer a way to equilibrate such systems much faster by bypassing the real-time dynamics. MC moves can rearrange polymer configurations in leaps, rather than tracking the slow diffusive motion of every monomer. This allows MC to sample the relevant region of configuration space in significantly fewer steps, achieving statistical equilibrium in cases where pure MD would be impractically slow.

By combining MC and MD, one can leverage the strengths of both methods. MC can be used to equilibrate the system and even to explore configurational transitions that are rare, while MD can then refine the behavior and provide dynamical insight. For example, MC techniques are very efficient for mapping out free-energy profiles along slow collective coordinates or order parameters (such as a chain folding angle or an end-to-end distance) by effectively sampling those rare transitions many times. This is something that could take an exceedingly long simulation time to observe even once in an unbiased MD run. With the free-energy landscape in hand (e.g., identifying energy barriers and stable states), one can then use MD to study the dynamics on that landscape (for instance, running MD to see how a polymer transits between states or to calculate rate constants for transitions using methods like umbrella sampling or transition state theory). In practical terms, an MC→MD workflow might involve using Monte Carlo to rapidly produce a well-equilibrated, statistically representative polymer melt configuration, and then switching to MD to simulate how that melt responds to perturbations or evolves over (shorter) time periods. This hybrid approach yields both efficient sampling (from MC) and accurate time evolution (from MD), allowing researchers to obtain equilibrium properties and dynamic properties in a fraction of the computing time that a brute-force MD-alone approach would require.

3.3 Fundamentals of MD Simulations

3.3.1 Newtonian Mechanics

This powerful method is of great importance in studying various processes (and phenomena) at the molecular level in science and engineering. MD simulations are rooted in classical Newtonian Mechanics. The concept of molecular dynamics is to simulate a system comprising molecules with known interactions between the particles. By utilizing intermolecular potential, we calculate the forces acting on particles and solve Newton's equation of motion,

$$m_i \frac{d^2 \mathbf{r}_i}{dt^2} = \mathbf{F}_i \tag{3.8}$$

where $\mathbf{F}_i = -\nabla_i U$ is the force acting on particle i given by the negative gradient of the potential energy. This equation $\mathbf{F}_i = -\nabla_i U$ is the fundamental starting point for MD [70]. The task of an MD simulation is to integrate these equations of motion forward in time, thus generating a trajectory $\mathbf{r}_i(t)$ for all particles i in the system.

3.3.2 Integration of Equation of Motion: The leap-frog Algorithm

Because the equations of motion have no analytical solution for many interacting particles, we resort to numerical integration algorithms. A popular integration scheme, which was used as an integrator in the present study, is the leap-frog algorithm. Leap-frog integration is a variant of the Verlet family of integrators that updates velocities and positions in a staggered (leap-frog) manner. Specifically, velocities are computed at half-time steps (e.g. $t + \Delta t/2$) and positions at full time steps (e.g. $t + \Delta t$) [32]. In practice, one iteration of the leap-frog algorithm will compute the velocity $\mathbf{v}_i(t + \frac{1}{2}\Delta t)$ from the forces at time t, then use that to update the position $\mathbf{r}_i(t + \Delta t)$. By "leap-frogging" over the integer time steps, the velocities and positions remain out of phase by half a step, hence the name. This method is time-reversible and symplectic, which means it conserves energy well for conservative forces. The leap-frog (or closely related velocity-Verlet) integrator is widely used in MD because of its simplicity and stability [71]. As long as a sufficiently small time step Δt (on the order of 1-2 fs for atomistic simulations) is chosen, the algorithm can accurately integrate the motions of polymer segments without significant drift in total energy.

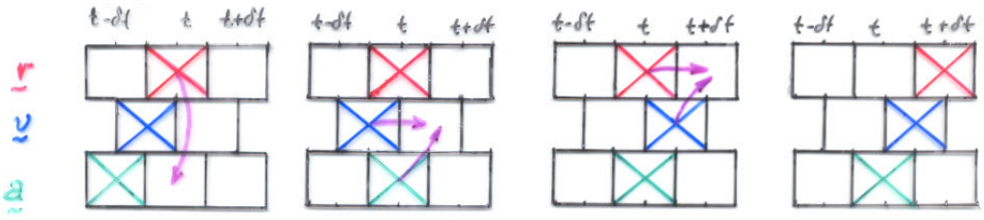


Figure 3.3: Schematic of the leap-frog method. Positions are evaluated at integer time steps, while velocities are evaluated at half-integer steps [7].

3.3.3 System Initialization

Before the actual simulation, the system needs to be initialized, meaning that initial positions and velocities should be assigned to atoms. The placement of the atoms on a lattice can be a starting point in order to acquire the positions. This has the disadvantage, though, that more time is required for the equilibration of the system. Allen and Tildesley note that using a high-symmetry initial placement can artificially prolong the equilibration, especially for macromolecules that need to disentangle [70]. To expedite equilibration, specialized amorphous packing methods are used for polymers. In this study, Scienomics's MAPS Amorphous Builder [72] was employed to generate amorphous PE configurations. This builder used a procedure akin to the method proposed by Theodorou and Suter [73], in which polymer chains are built within the boundaries of the simulation cell sequentially. The atoms in each chain are placed one by one, and the chosen position is accepted with a Boltzmann probability–of course, there should be no overlap between the particles and the placement of each one of them should meet the imposed constraints.

Once the positions are assigned, initial velocities must be generated. Velocities are typically sampled from the Maxwell-Boltzmann distribution corresponding to the desired temperature T [32].

$$p(u_i) = \sqrt{\frac{m_i}{2\pi k_B T}} \exp\left(-\frac{m_i u_i^2}{2k_B T}\right) \tag{3.9}$$

where k_B denotes the Boltzmann factor, m_i the mass of atom i, T is the temperature and u_i is the velocity component of atoms i along a certain direction x,y,z.

3.3.4 Energy Minimization

Even with clever initial positioning, there will be residual strain or small atomic overlaps in the configuration. Therefore, it is common to perform an energy minimization before starting the MD production run [74]. Energy minimization is to find a nearby local minimum of the potential energy U by adjusting atomic coordinates. Methods such as steepest descent and conjugate gradient are typically employed for this purpose. In the steepest descent algorithm, atoms are moved iteratively in the direction of the force (negative energy gradient), which guarantees a decrease in energy in each step [75]. The algorithm is robust but can be slow to converge when close to the minimum. Conjugate gradient is faster since it takes into account the history of the gradient to get an optimal descent direction, converging in fewer steps for well-behaved potentials [75]. One typically uses steepest descent for a few hundred steps to quickly relieve the biggest forces (as it is more stable when far away from the minimum), and then switches to conjugate gradient for fine relaxation. In minimizing the energy, we remove any highly unfavorable contacts that would produce large forces and instability in the MD integrator.

3.3.5 Periodic Boundary Conditions (PBC)

In a simulation, for practical purposes, a few thousand or millions of atoms are simulated. This is done because of restrictions on memory and computational time. For this reason, in order to mimic the properties of a material on larger scales, the periodic boundary conditions are used. Periodic boundary conditions are employed to eliminate surface effects by surrounding the simulation box with copies of itself in all directions. In a PBC setup, the primary solution cell is replicated to form an infinite tiling of space. The moment a polymer chain or segment crosses one of the primary cell boundaries, it enters from the opposite boundary. In other words, an atom leaving the simulation box on the right-hand side returns on the left-hand side with the same velocity, and similarly for top-bottom and front-back faces [7, 70]. What is created is the illusion that the simulation is part of an infinite periodic lattice of identical systems. As such, a chain in the central box may interact with image atoms of a neighboring chain that has exited the box, maintaining continuity of interactions.

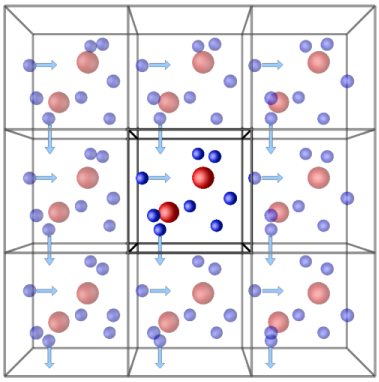


Figure 3.4: The central simulation box (outlined in black) is surrounded by periodic image boxes. When a particle (red or blue sphere) leaves one side of the primary box, it re-enters from the opposite side (blue arrows indicate the trajectory of a moving particle). Thus, each molecule always finds a neighbor even at the boundaries, as it effectively interacts with an infinite array of images [8].

An important convention for applying periodic boundary conditions is the minimum image convention. Since the simulation only keeps track of the primary cell explicitly, we must compute interatomic distances by considering each atom and the nearest image of every other atom. For example, if two monomers are far from each other across the boundary, the distance is computed to the image that lies inside the central cell (or close to it) rather than the possibly larger distance in the same cell. The minimum image convention means each particle interacts with no more than one image of any other given particle, namely the closest one. For the minimum image convention to be satisfied in a cubic box, the cut-off distance of the inter-molecular interactions r_c must be equal or smaller than half the box side length $r_c \leq L/2$. [7, 70]. This ensures that a particle does not interact with more than one periodic image of another particle, avoiding double-counting interactions. Allen and Tildesey emphasize this criterion as essential for the correctness of MD with PBC.

3.4 Force Field and Computational Efficiency

Accurate MD simulations require a reliable description of interatomic forces, provided by a force field. The force field defines the functional form of the potential energy $U(\mathbf{r}^N)$ and the parameters (force constants, equilibrium values, etc.) for the specific material. In this work, we use the TraPPE-UA force field to model polyethylene [31, 32]. TraPPE (Transferable Potentials for Phase Equilibria) is a family of force fields designed to be transferable across different but related systems, especially for phase equilibrium properties. The TraPPE-UA (United Atom) model treats –CH_2– and –CH_3 group in polyethylene as a single interaction site (a united atom), clustering the hydrogen atoms with the carbons [76]. This is a simplification that reduces the number of particles and degrees of freedom, significantly improving computational efficiency for long-chain hydrocarbons, while still capturing the overall chain geometry and dispersive interactions.

3.4.1 Bonded Interactions

In this Thesis, for all MD simulations of PE melts, we constrained all C-C bond lengths to a fixed value [31, 32, 76]. Bond angles (the C-C-C angles along the backbone) are governed by a harmonic bending potential,

$$U_{\text{angle}} = \frac{1}{2} k_\theta \left(\theta_{ijk} - \theta_o\right)^2 \tag{3.10}$$

where θ_{ijk} is the bond angle between atoms i, j and k, θ_0 is the equilibrium bond angle and k_θ is a constant.

Dihedral angles (torsion around C-C bonds) are crucial for polymer conformational flexibility. TraPPE-UA uses a variety of functions, primarily based on the cosine relationship. A common form used is

$$U_{\text{RB}}(\phi_{ijkl}) = \sum_{n=0}^{5} a_n (\cos \phi_{ijkl})^n, \tag{3.11}$$

where ϕ_{ijk} is the dihedral angle formed by four atoms i, j, k, l and a_n is a constant.

3.4.2 Non-Bonded Interactions

These account for van der Waals and, if acceptable, electrostatic forces between atoms on different chains or distances along the same chain. Polyethylene is a nonpolar hydrocarbon, so the dominant non-bonded interaction is the dispersive van der Waals attraction, well-described by a Lennard-Jones (LJ) 12-6 potential. In TraPPE, each united atom (CH2 or CH3) interacts via LJ parameters that have been optimized for n-alkane thermophysical properties [32, 76]. The LJ potential between two sites i and j is,

$$U_{\text{LJ}}(r_{ij}) = 4\epsilon_{ij} \left[\left(\frac{\sigma_{ij}}{r_{ij}} \right)^{12} - \left(\frac{\sigma_{ij}}{r_{ij}} \right)^{6} \right] \tag{3.12}$$

where r_{ij} is the distance between the two interacting sites, ϵ_{ij} is the depth of the potential well (interaction strength), and σ_{ij} is the finite distance at which the Lennard–Jones potential crosses zero. In our simulations, we apply tail corrections beyond r_c to account for the negligible long-range dispersion contributions. The TraPPE-UA force field parameters, including ϵ and σ, were taken from the literature–in fact, our simulations used the values published by Pütz et al. [77] for improved TraPPE-UA parameters.

3.4.3 Other Force Fields for PE Melts

It is worth noting that alternative force fields exist for polyethylene and may be used depending on the desired accuracy or scale. For instance, all-atom force fields such as OPLS-AA treat every hydrogen explicitly and include detailed torsional potentials and partial charges [78]. All-atom models can capture subtle stereochemical effects but are more computationally demanding (3x more particles than UA). Another class of force fields, such as COMPASS [79] or GROMOS [80], has parameters for polyethylene as well. Each force field has its own strengths. All models can predict vibrational spectra and local packing in detail, while united-atom or coarse-grained models allow reaching larger lengths and time scales. In this thesis, we chose TraPPE-UA because it offers a good balance of accuracy and efficiency for PE melts [31]- it has been shown to reproduce liquid densities and structure of alkanes reasonably well [81] while keeping the computational cost manageable by reducing the atom count.

3.5 Neighbor Lists and Computational Efficiency

A major computational expense in MD is evaluating the non-bonded pairwise forces, which naively scale as $O(N^2)$ for N particles. In a polymer melt of thousands of atoms, checking every pair each time step is prohibitively slow. To accelerate these calculations, MD codes use neighbor lists (also known as Verlet lists) [70, 71]. The concept is to avoid computing distances for pairs that are definitely outside the cutoff r_c. At the start of the simulation (or periodically), a neighbor list is built for each atom–all other atoms within a larger radius $r_{\text{list}} > r_c$ are listed as possible interaction partners. The difference $r_{\text{list}} - r_c$ is a skin margin to account for the fact that atoms move over time. For each time step, instead of looping over all N atoms for each i, the program only loops over the neighbors in i's list (which is much shorter on average). This reduces the workload drastically, to on the order of $O(Nn_{\text{neigh}})$ where n_{neigh} is the average number of neighbors per atom (related to the local density and volume of the sphere of radius r_{list}) [70, 71]. Every few time steps, the neighbor lists are rebuilt or updated if any atom has moved more than the skin distance (so that no possible new collision is missed). Using Verlet neighbor lists can bring the cost of force calculations down near $O(N)$ for larger systems, which is essential for scaling to bigger polymer melts.

Chapter 4

Methodology

This chapter details the methodological framework used for molecular dynamics (MD) simulations, from the initial preparation to the final data analysis, for quiescent (no-flow) and flow-induced crystallization of PE melts. First, the simulated polydisperse PE systems employed in this research, and the equilibration procedure that yields thermodynamically stable molten configurations of polydisperse PE chains are described. Next, the simulation protocols for production runs are explained for both flow-induced (uniaxial-deformation) and quiescent (zero-flow) crystallization conditions. Then, how the degree of crystallinity is quantified, with the orientational order parameter, is explained. Finally, the post-processing analysis technique is presented, including a method to characterize the time-evolution of semi-crystalline morphology and quantify nucleation and growth kinetics during these non-equilibrium transformations in the polymer melt.

4.1 System Studied

Two different PE melt systems were studied in this work to examine how molecular weight and protocols of crystallization influence crystallization kinetics. The first system consists of 100 polymer chains with an average of 1,000 methylene units per chain, and the second contains 50 chains with an average of 2,000 methylene units per chain. With a polydispersity index (PDI) of 1.08 that characterizes the molecular weight distribution of the chains, each system consists of around 10,000 methylene units in total. All MD simulations employed the TraPPE united atom (UA) force field (as described earlier in Chapter 3) for both initial system construction and subsequent dynamics. The UA representation was chosen to make the long timescales of the simulation computationally feasible, while still maintaining the required thermodynamic and structural molten PE behavior as observed in experiments [82, 83]. United atom force fields are known to be unable to represent explicitly the exact

orthorhombic unit cell of crystalline PE, but the TraPEE-UA parameterization has already been shown in other studies to successfully capture crystallization trends [84, 85, 38].

4.2 Pre-Processing Protocol

During the pre-processing, the initial configurations of all PE systems were constructed at 450K utilizing the amorphous cell builder module of Scienomics' MAPS software [72], in a cubic cell with periodic boundary conditions being applied in all directions. Each monodisperse initial configuration was then energy-minimized using the GROMACS package [69] in order to eliminate any steric overlaps caused by the initial packaging of the chains. To generate the target polydispersity molecular weight distribution, a home-built Monte Carlo (MC) sampling procedure with uniform chain length selection was implemented, after methodologies in previous studies on united atom (UA) polyethylene melt equilibration [86]. Specifically, two different systems were generated;

(i) A system of number-averaged molecular weight $M_n = 14{,}000\,\mathrm{g/mol}$ (referred to as 1K or C1000), having chain lengths uniformly distributed between 500–1,500 UA units, leading to $M_w \approx 12{,}963\,\mathrm{g/mol}$ (PDI = 1.08).

(ii) A system of $M_n = 28{,}000\,\mathrm{g/mol}$ (referred to as 2K or C2000), with uniformly distributed chain lengths between 1,500–2,500 UA units, which resulted in $M_w \approx 25{,}926\,\mathrm{g/mol}$ (PDI = 1.08).

After adjusting the chain length to achieve polydispersity, the systems were further equilibrated by performing MD simulation in the NPT ensemble for 20 ns, where temperature and pressure were kept constant and equal to 450 K and 1 atm, respectively. The root mean squared radius of gyration $\sqrt{\langle R_g^2 \rangle}$ of the 2K (C2000) PE melt system at 450K was approximately 82 Å, the average density of the system was 0.77 g/cm^3, and the average cubic cell simulation length L_0 was approximately 147.50 Å.

4.3 Simulation Protocol

While the production simulations were being conducted, a combinatorial parametric approach was applied to systematically examine both molecular weight and uniaxial deformation effects on crystallization kinetics. The two pre-described polyethylene melts (number average chain lengths of 1,000 and 2,000 methylene units, respectively) were exposed to two types of crystallization conditions: quiescent (zero-flow) and flow-induced (uniaxial deformation). Having a double-axis experimental design (varying both the chain length and the flow conditions) enables a direct comparison of the following:

- **Molecular weight effects** —how polymer chain length influences nucleation barriers and crystallization kinetics, and

- **Flow-induced effects** — how an imposed deformation increases or otherwise alters the formation of the crystalline phase,

thereby helping to resolve the competing thermodynamic and kinetic contributions to semi-crystalline microstructure formation and further development. All the simulations were carried out within the GROMACS environment employing the TraPPE-UA force field. A time step of $\Delta t = 2$ fs was used throughout, which provided a balance between numerical stability and computational efficiency.

4.3.1 Quiescent Conditions

Under quiescent conditions, the equilibrated melt configurations were cooled down to 340 K, applying a constant fast cooling rate of 10 K/ns in order for any premature crystallization to be prevented during this initial cooling process. Once the systems had reached 340K, it was maintained at this temperature (without any external perturbations) to observe crystallization in non-deformed conditions.

4.3.2 Flow-induced Conditions

For the flow-induced crystallization simulations, we implement a uniaxial drawing protocol that mimics uniaxial elongation process. In particular, after the same thermal conditioning as described earlier in the quiescent case, we applied a constant uniaxial deformation with a drawing rate,

$$\dot{\varepsilon} = 10^7 \text{ s}^{-1} = \frac{L_x(t) - L_x(0)}{t\, L_x(0)} = \dot{\lambda} \tag{4.1}$$

where t is the time needed to deform the sample from $L_x(0)$ to $L_x(t)$, and L_x is the length of the simulation box in the x-direction. Also, the degree of elongation is characterized by the time-dependent draw ratio defined as,

$$\lambda(t) = \frac{L_x(t)}{L_x(0)}, \tag{4.2}$$

During this drawing process, a constant ambient pressure of 1 atm was held constant in the y and z directions. As a consequence, the film thickness diminished as drawing progressed.

4.4 Post-Processing Protocol

4.4.1 Estimation of Degree of Crystallinity

A key quantity in our simulation analysis is the time-dependent degree of crystallinity, $X_c(t)$, and its evolution under different crystallization conditions. There are many ways to define X_c based on density, enthalpy, and orientation. In this work, a method proposed by Takashi Yamamoto [87] was used. In particular, at each time step of the simulation, the simulation

box is divided into small cubic sub-cells of side length,

$$L_{\text{cell}} = 2\sigma_{\max} = 2 \times 3.95 \text{ Å} \approx 7.9 \text{ Å}, \tag{4.3}$$

where $\sigma_{\max} = 3.95$ Å is the effective segment diameter of a CH_2 group in our UA model. Within each sub-cell, we computed an orientational order parameter to quantify local chain alignment. For each sub-cell, an orientational order parameter is computed to quantify local chain alignment. This order parameter is defined as follows,

$$P_2 = \left\langle \frac{3\cos^2\theta_{ij} - 1}{2} \right\rangle, \tag{4.4}$$

where θ_{ij} is the angle between a given pair of chord vectors, and the average $\langle\cdot\rangle$ is taken over all possible pairs of chord vectors within the cell. It should be noted that a chord vector is defined as the unit vector connecting the midpoints of two adjacent skeletal bonds; it is assigned to the cell where the middle united atom, i.e., the shared atom between the two adjacent bonds, belongs.

According to Yamamoto's criterion, a sub-cell is considered "crystalline" if its local orientational order parameter exceeds a certain threshold,$P_2 > 0.7$. Finally, the overall degree of crystallinity $X_c(t)$ at time t is estimated as the percentage of the sub-cells with $P_2 > 0.7$

The reliability of this orientation-based crystallinity measurement has been previously established in a similar study conducted by Anogiannakis et al [31], who described a thorough methodological framework that also encompassed enthalpy and density-based definitions to estimate the evolution of $X_c(t)$. In order to test further the robustness of this orientational-based method, they compared the temporal evolution of $X_c(t)$ as derived from three independent methodologies.

- **Orientation-based method (Yamamoto's approach)**

- **Enthalpy-based definition** — the original thermodynamic definition of the degree of crystallinity:

$$X_{c,\text{enthalpy}} = \frac{H_{\text{semi}} - H_{\text{amor}}}{m_{\text{amor}} \cdot (-\Delta H_f)} \tag{4.5}$$

  where H_{semi} is the enthalpy of the semicrystalline sample at a given time, H_{amor} is the enthalpy of an equal mass of the polymer in a completely amorphous state, m_{amor} is that mass, and ΔH_f is the specific enthalpy of fusion (melting) of a perfect PE crystal (determined using the same TraPPE-UA force field).

- **Density-based definition** — this method estimates the degree of crystallinity through density using the following relation:

$$X_{c,\text{density}} = \frac{\rho_{\text{semi}} - \rho_{\text{amor}}}{\rho_{\text{cryst}} - \rho_{\text{amor}}} \tag{4.6}$$

where ρ_{semi} is the density of the partially crystallized sample, ρ_{amor} is the density in the purely amorphous state, and ρ_{cryst} is the density of a perfect polyethylene crystal.

Following the above methodological framework, we constructed a similar graph to that described in their study. Figure 4.1, shows the evolution of the orientation-based degree of crystallinity for one of our 2K PE systems under stretching conditions ($\dot{\varepsilon} = 10^7$ s^{-1}) denoted by the black curve to be in good agreement with the evolutions of both enthalpy-based and density-based degrees of crystallinity, denoted with the blue and red curves, further validating the robustness of the first method.

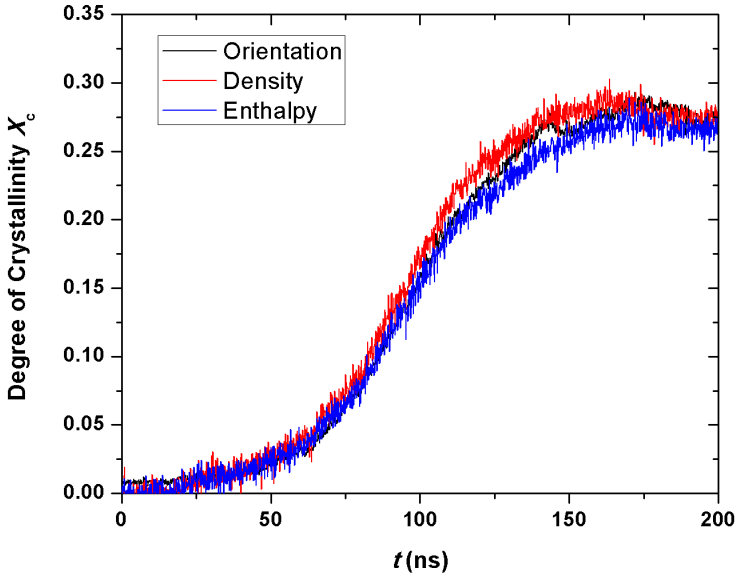


Figure 4.1: Time evolution of the degree of crystallinity X_c using three different methods: Yamamoto's orientational-based method (black line), density-based definition (red line), and thermodynamic enthalpy-based definition (blue line). The plot corresponds to one 2K PE system, which is drawn at a constant strain rate of $\dot{\varepsilon} = 10^7$ s^{-1} at $T = 340$ K.

4.4.2 Kinetic Analysis

Aside from estimating overall crystallinity, the crystallization kinetics were also examined to characterize the nucleation and growth of crystals. During both of our drawing and quiescent simulations, a semi-crystalline morphology develops in the end. Beginning from purely amorphous melt systems, after a specific time, several crystal nuclei are formed. Some of them dissolve and return to the amorphous phase, but few manage to become large enough, reaching a critical nucleus size and continuing to grow to well formed crystallites.

To analyse the kinetics of nucleation and growth from the aspect of quantity, we applied a mean first passage time analysis (MFPT) focusing on the largest nucleus of our systems. MFPT is a method in which nucleation is considered to be an activated process which involves surmounting a free energy barrier. There is a reaction coordinate that defines the conditions of the process, which is the size of the largest cluster $n_{\max}$ in our case.

In other words, for every potential size of the nucleus on the X-axis, the MFPT curve indicated how long, on average, we had to wait for the largest nucleus to first attain that size. In particular, based on either our stretched or our quiescent simulations, we extract an averaged characteristic plot of the mean time needed for the largest nucleus present in the system to achieve a specific size $n_{\max}$. We fit an analytical MFPT model to this plot in order to extract meaningful kinetic parameters. The form of the MFPT function is as follows :

$$\tau(n_{\max}) = \frac{1}{2}\tau^* \left[1 + \operatorname{erf}\left(Z\sqrt{\pi}\,(n_{\max} - n^*)\right)\right] + G^{-1}(n_{\max} - n^*)\, H(n_{\max} - n^*) \tag{4.7}$$

where τ^* is the induction time, i.e, the time that needs to elapse before a critical nucleus event occurs, n^* is the critical nucleus size, Z is the Zeldovich factor, which corresponds to the probability that a nucleus of size near n^* will survive and not dissolve into the melt phase, G is the growth rate and H is the Heaviside function. A continuous approximation of Eq 4.7 that is more amenable to fitting is

$$\tau(n_{\max}) = \frac{1}{2}\tau^* \left[1 + \operatorname{erf}\left(Z\sqrt{\pi}\,(n_{\max} - n^*)\right)\right] + \frac{1}{2}G^{-1}(n_{\max} - n^*)\left[1 + \operatorname{erf}\left(C(n_{\max} - n^*)\right)\right] \tag{4.8}$$

where $C = 10000$ is a large positive number. Eq 4.8 enables the smooth approximation of the Heaviside function H by the error function.

The simplified formulation of the MFPT function follows the approach of Yi et al. [38], who introduced an additional term in the MFPT expression to account for finite crystal growth rates of post-critical nuclei, when the condition $G \gg n^*/\tau^*$ is not satisfied. Finally, the induction time τ^* is connected with the nucleation rate I via equation 4.9,

$$I = \frac{1}{V\,\tau^*}, \tag{4.9}$$

where V is the volume of the simulation cell in the amorphous state.

Chapter 5

Results & Discussion

In this section, the crystallization kinetics of polyethylene (PE) is researched under two protocols—flow induced and quiescent—for a simulated system of 50 PE chains with an average of 2,000 CH_2 units. First, findings concerning the crystallinity and nucleation behavior under external flow (uniaxial elongation) and under quiescent conditions at the same subcooling are discussed and compared. Subsequently, these results are compared against those of a similar work by Dr. Anogiannakis and Mr. Venetsianos, PhD candidate, using a system of shorter chains (100 PE chains with $\sim$ 1,000 CH_2 units per chain).

5.1 System of 50 C2000 chains

5.1.1 Degree of Crystallinity

Flow-Induced Conditions

Figure 5.1 and Figure 5.2 show the evolution of the degree of crystallinity (X_c) upon stretching versus time. Ten independent molecular dynamics (MD) runs were performed under identical initial conditions; the system was quenched from the melt to 340 K with a controlled cooling rate of 10 K/ns and subsequently subjected to uniaxial extension at a high strain rate of 10^7 s^{-1}, as described above in the Methodology section. The individual crystallinity trajectories in **Figure 5.1** exhibit a very steep rise and nearly overlap, indicating that there exists a very narrow distribution of nucleation times from run to run. This suggests that, under high extensional flow, nucleation and growth are highly reproducible and rapid, with statistically valid results even from a relatively small number of runs. Along with that, the averaged crystallinity curve in **Figure 5.2**, from all ten simulations, highlights the principal stages of morphological development. In both Figures 5.1 and 5.2, there are **three distinct regions** to be identified in the plot of degree of crystallinity X_c vs time. The first is an **induction period**, in which no detectable increase in X_c is observed. This is

followed by a **rapid growth stage**, where the degree of crystallinity rises sharply; initiation of this stage defines the induction time τ^*—the time when the first stable crystal nucleus appears and triggers rapid crystallization. Finally, there is a **plateau region** at longer times, where the X_c levels off to a terminal value. Due to periodic boundary conditions applied in our simulations and the fact that no secondary crystallization occurs under the conditions considered here, the crystallinity reaches the so-called terminal crystallinity.

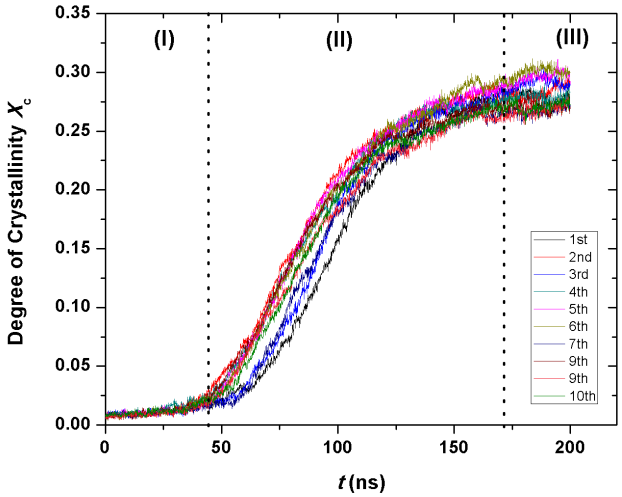


Figure 5.1: Time evolution of the degree of Crystallinity X_c from 10 independent MD simulations of polydisperse 2K PE system under stretching conditions.

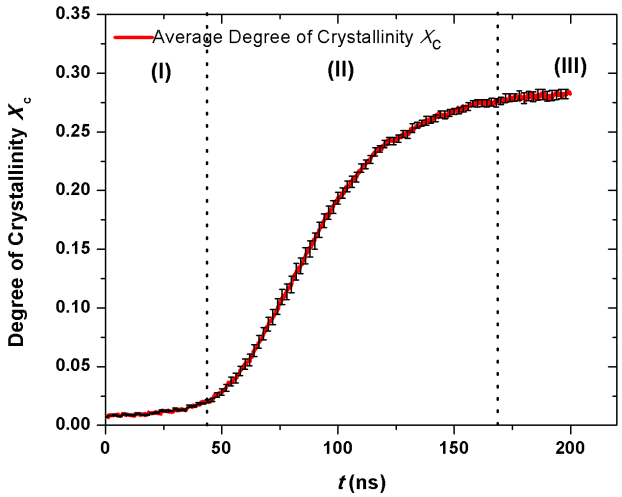


Figure 5.2: Mean crystallization curve $X_c(t)$ for the polydisperse 2K PE system under stretching conditions, calculated as the average of 10 independent MD simulation runs. The curve exhibits a characteristic sigmoidal shape: an initial lag (induction period), followed by a steep rise as crystallization proceeds, and finally a plateau.

From **Figure 5.2**, it is estimated that the induction time under flow is approximately $\tau^* \approx 45$ ns, based on the point at which the averaged X_c curve begins its steep rise. Interestingly, this flow-induced induction time is extremely short–of the order of only a few tens of nanoseconds–reflecting the efficacy of deformation in promoting crystallization. The presence of an induction period followed by a sudden increase in crystallinity is consistent with observations from other MD studies of stretch-induced polymer crystallization [31, 32, 66, 84, 87]. Yamamoto et al. [87], for example, reported that a rapidly elongated PE melt exhibits an initial waiting period for critical nucleation, followed by a stage of independent lamellar growth with a sharp increase in crystallinity, and finally a slowdown as growing crystallites impinge on each other, analogous to the three-stage behavior we observe. The fast crystallization in our stretched simulations is a direct consequence of flow-alignment of the chains, which greatly facilitates nucleus formation and growth. Indeed, external deformation can strongly promote nucleation by reducing the entropic barrier and helping in the alignment of chain segments [31]. In the literature, flow-induced crystallization is well-known to shorten induction time and increase overall crystallization rates relative to quiescent conditions. Our simulations under high strain rate are in line with these trends; the polymer melt crystallized almost immediately once stretching was applied, and the narrow spread between individual runs indicates that the stochastic nature of nucleation is largely overcome by the strong driving force of flow.

Quiescent Conditions

Figure 5.3 and **Figure 5.4** present the corresponding crystallinity evolution results for the quiescent crystallization simulations. Applying this protocol, twenty runs were conducted (more trajectories were used to improve statistical sampling, as more variability was expected in the absence of flow). Each system was quenched from 450K to 340K at the rate of 10K/ns and then kept at 340K without any applied deformation so that crystallization could proceed through homogeneous nucleation driven solely by thermal fluctuations and chain mobility. The degree of crystallinity versus time for each of the 20 individual quiescent runs is presented in **Figure 5.3**. There is clear spreading in the trajectories; some runs remain amorphous for an incredibly long time before nucleation, whereas others crystallize earlier, resulting in a broad distribution of nucleation times. This wide scatter indicates the extremely stochastic nature of homogeneous nucleation in polymers. In fact, even with 20 independent simulations (each up to 1.7 µs), there is significant run-to-run variability, so that an even larger number of samples may be required in order to have the nucleation statistics completely converged. **Figure 5.4** shows that the averaged crystallinity curve remains near zero for an extended period compared to the flow-induced conditions. The whole process of crystallization under quiescent conditions is very much slower compared to flow, as expected. The construction of Figure 5.4 was carried out by identifying the onset of nucleation in each simulation (the point just before the sharp rise in X_c) and shifting the time axis so that this point was set to zero. This procedure allowed us to calculate the mean crystallinity curve based on the individual curves from Figure 5.3 while taking into account only the crystal

growth behavior. In the absence of flow, chain segments need to wait for random thermal motion to align and attach them to a nascent crystal, and thus the kinetics are limited by the rarity of a sufficient density fluctuation to form a stable nucleus. Indeed, it has been observed that at the same temperature (340K), a quiescent supercooled melt exhibits significantly delayed crystallization response compared with a drawn melt. This result is in agreement with the established understanding that, without an external orientation field, polymer nucleation would be a rare event and could be very slow on MD time scales [57]. As Luo and Sommer [57] found, dense entanglement can slow nucleation down because chain mobility to form an ordered nucleus is restricted when chains are topologically constrained. We observe a prolonged induction period and broadly distributed nucleation times under zero flow conditions.

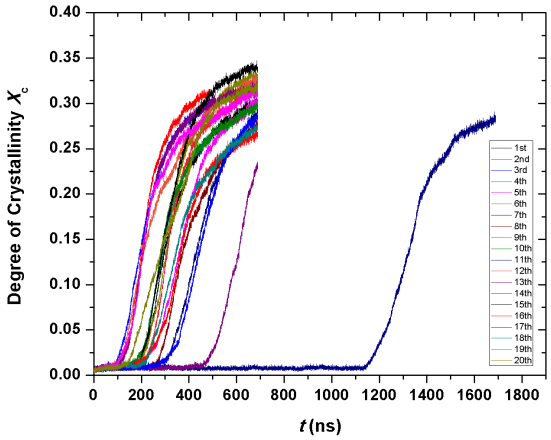


Figure 5.3: Time-resolved crystallinity trajectories $X_c(t)$ from 20 independent MD simulations of polydisperse 2K PE system under quiescent conditions. Each $X_c(t)$ reflects the stochastic nature of homogeneous nucleation, with the induction time for nucleation varying significantly across runs.

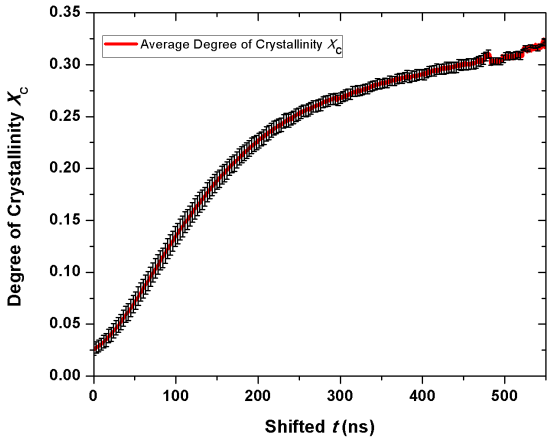


Figure 5.4: Average crystallization curve $X_c(t)$ for the polydisperse 2K PE system under quiescent conditions, derived from the trajectories in Figure 5.3.

The induction time (time when X_c begins to rise) under quiescent conditions is roughly estimated from **Figure 5.4** on the order of $\tau^* \approx 240 - 245$ ns (time when X_c begins to rise). This induction time is approximately an order of magnitude greater than the flow-induced one (45ns). This significantly larger τ^* may reflect the higher free energy barrier for spontaneous nucleation; the supercooled melt can remain in its pre-nucleation state for several hundred nanoseconds prior to the formation of the first critical nucleus. While a timescale of 240- 245ns could, at first glance, appear short relative to experimental observation where nucleation typically occurs over microseconds to milliseconds, it should be stated that experimental studies on linear polyethylene are carried out at temperatures much higher than our simulated temperature (340K). Consequently, nucleation events in our systems can be seen to happen on comparable shorter timescales. All 20 of our simulations did eventually nucleate a crystal within the 1.7 µs window, which indicates that 340K is a deep enough subcooling to induce nucleation within a reasonable MD time scale. The three-region crystallization profile discussed above is also observable under quiescent conditions, but stretched out over a much longer time frame. Overall, quiescent simulations demonstrate that, without flow, crystallization of polydisperse PE is slower and more variable, consistent with the classical view of homogeneous nucleation being a rare, thermally activated process.

5.1.2 Kinetic Analysis

To quantitatively analyze the crystallization kinetics observed above, we applied a **mean first-passage time (MFPT)** analysis [88] (after Wedekind et al.'s method) to the simulation data. This approach considers the size of the largest crystalline cluster in the system as a function of time and uses the statistical distribution of the first-passage times of various size thresholds to extract the kinetics of nucleation. In particular, the MFPT method allows us to estimate the critical nucleus size n^* and the induction time τ^* more rigorously by fitting the MFPT curve to the theoretical form expected for nucleation processes. The critical size n^* corresponds to the number of monomer units (CH_2 groups) in the largest cluster at the top of the nucleation free energy barrier, and τ^* corresponds to the mean time required to form such a nucleus. Additionally, the inverse of the slope of the MFPT curve beyond the induction period can be related to the crystal growth rate G once nuclei become supercritical. Below, we present the MFPT analysis results for the flow-induced and quiescent cases, which provide a consistent set of kinetic parameters to compare the two protocols.

Flow-Induced Conditions

Figure 5.5 shows the MFPT plot of the largest nucleus size for the flow-induced crystallization simulations, averaged over the 10 independent stretched trajectories. The open circles in Figure 5.5 represent the simulation MFPT data (i.e., the averaged time by which a cluster of given size is first observed), and the solid red line is the best theoretical MFPT curve. From this analysis, the critical nucleus size and induction time under flow are determined to be $n^* = 107.23 \pm 3.3$ (in units of CH_2 monomer count) and $\tau^* = 43.9 \pm 0.45$ ns, respectively.

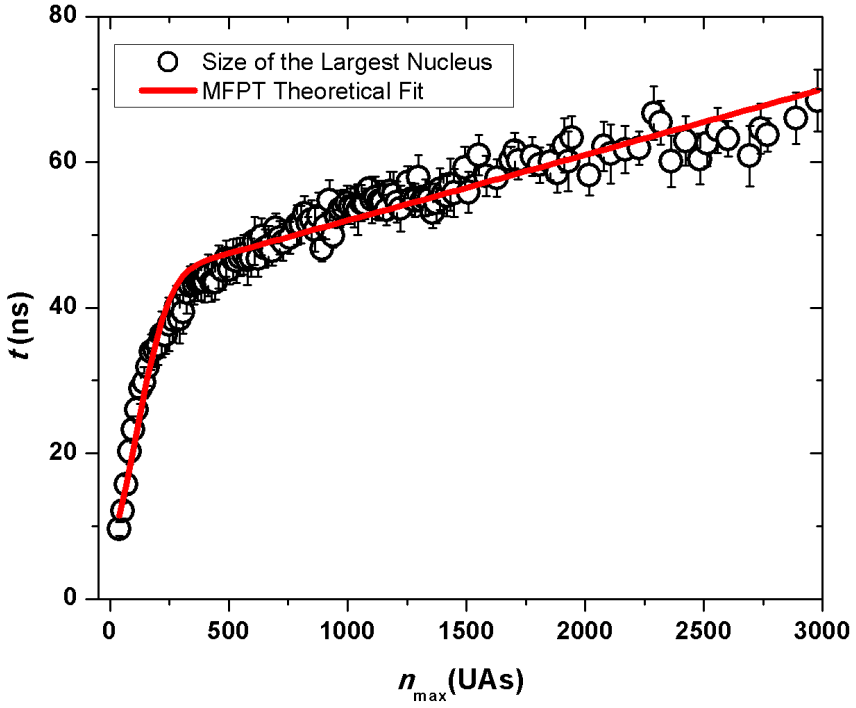


Figure 5.5: The mean first-passage time (MFPT) of the maximum nucleus size $n_{\max}$ for 10 MD simulations of a system of 50 polydisperse PE chains quenched from 450 K to 340 K and then stretched (flow-induced crystallization). The open circles represent the simulation MFPT data points, and the solid red line corresponds to the fitted MFPT theoretical curve. Error bars represent the standard error of the mean (SEM) of the passage time for each $n_{\max}$.

τ^* (ns)	G (UAs/ns)	n^* (UAs)	Z
43.91 ± 0.45	110.86 ± 4.45	107.23 ± 3.30	$0.00372 \pm 2.06 \times 10^{-4}$

Table 5.1: Mean values of induction time (τ^*), growth rate (G), critical nucleus size (n^*), and Zeldovich factor (Z) from 10 independent samples.

Wedekind et al.'s MFPT method thus quantitatively confirms what was qualitatively concluded from the crystallinity curves: under flow, the critical nucleus contains on the order of ~ 107 methylene units, and the time to nucleation is on the order of tens of nanoseconds. Figure 5.5 (and the extracted τ^*) merely confirms the above observation from the crystallinity-versus-time plot. In fact, the induction time calculated from the MFPT analysis ($\tau^* \approx 43.9$ ns) is in excellent agreement with the induction time estimated by eye from Figure 5.2 ($\sim$45 ns). This consistency between different measurements (cluster-based MFPT and crystallinity-based metrics) ensures that our estimate of the induction time is robust and not an artifact of a particular analysis method. The critical nucleus size, $n^* \approx 107$, under flow conditions, is significantly smaller than what is typically reported for quiescent homogeneous nucleation of polyethylene at similar supercoolings.

Yi et al. [38] found a critical nucleus of approximately 150 carbons for a quiescent PE melt at roughly 30% undercooling. The fact that in our flow case $n^* \approx 107$ could suggest that the applied deformation is successful in lowering the nucleation barrier so that a smaller critical cluster may become stable. That is consistent with the intuitive expectation that flow alignment will allow a small cluster to reach the level of ordering needed to sustain further growth. It is also in line with previous studies, where it was shown that flow can reduce the free energy barrier to nucleation, and consequently, accelerate the onset of crystallization [31].

Quiescent Conditions

The MFPT analysis for the quiescent simulations is shown in **Figure 5.6**, which plots the mean first-passage time of the largest cluster for the 20 independent quiescent trajectories. In this case, the data extend to much longer times, reflecting the slower kinetics. By fitting the MFPT data, we obtain a critical nucleus size of $n^* = 102.96 \pm 2.3$ monomer units and an average induction time of $\tau^* = 241.2 \pm 1.2$ ns for the quiescent case.

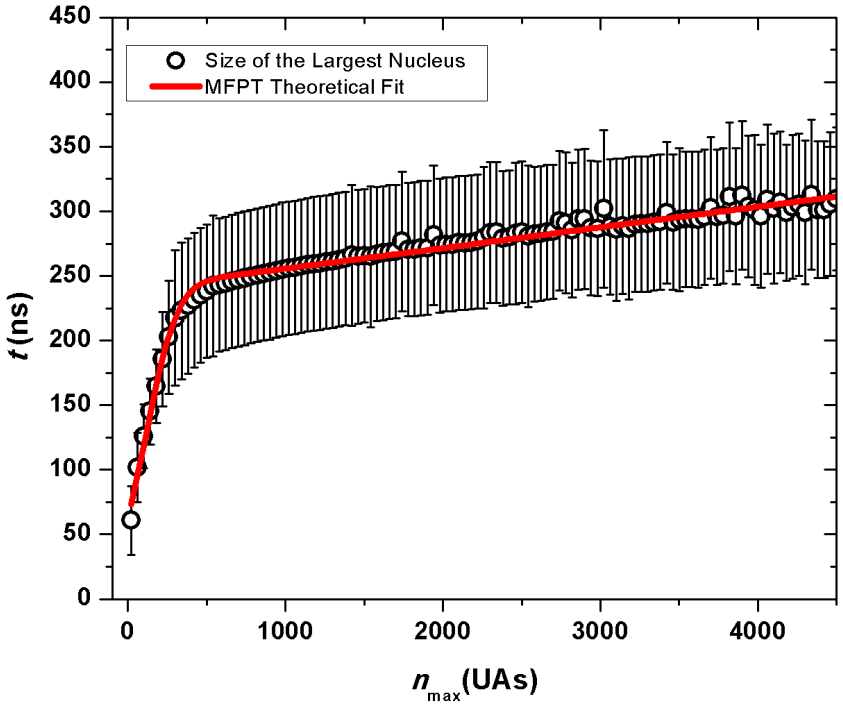


Figure 5.6: The mean first-passage time (MFPT) of the maximum nucleus size $n_{\max}$ for 20 MD simulations of a system of 50 polydisperse PE chains quenched from 450 K to 340 K. The open circles represent the simulation MFPT data points, and the solid red line corresponds to the fitted MFPT theoretical curve. Error bars represent the standard error of the mean (SEM) of the passage time for each $n_{\max}$.

τ^* (ns)	G (UAs/ns)	n^* (UAs)	Z
241.25 ± 1.20	62.60 ± 1.79	102.96 ± 2.31	$0.00248 \pm 7.45 \times 10^{-5}$

Table 5.2: Mean values of induction time (τ^*), growth rate (G), critical nucleus size (n^*), and Zeldovich factor (Z) from 20 independent samples.

These values quantitatively confirm the qualitative trends seen above: under quiescent conditions, the induction time is one order of magnitude higher than under flow-induced conditions. Yi et al. [38] determined nucleation rates for PE under similar supercooling that are comparable to mean waiting times on the order of 10^2–10^3 ns, in agreement with our findings. Thus, our simulations are in line with previous works in showing that homogeneous nucleation in polyethylene on the molecular scale requires hundreds of nanoseconds of fluctuation-driven ordering. The large difference between the quiescent and flow τ^* values (241 ns vs. 44 ns) demonstrates that flow enhances nucleation kinetics by roughly a factor of six in induction time—or conversely, by almost an order of magnitude in nucleation rate, since nucleation rate is inversely related to induction time for a given system size. Notably, the MFPT fits yield that the critical nucleus size n^* under flow is slightly bigger than in the quiescent case. This suggests that flow primarily accelerates the kinetics of reaching a critical nucleus but not the thermodynamics of nucleus size. It is worth noting that a similar study [31] under stretching conditions mimicking the industrial MDO process (instead of the uniaxial elongation in our study) indicated a slight decrease in n^* within the investigated strain rate range of $5 \times 10^6 - 10^8 \mathrm{s}^{-1}$. However, direct comparison is not easy, due to the different stretching protocols and the quite different timescales of the strain rates.

We do note that the MFPT-derived crystal growth rate G was higher under flow. In particular, under flow, G was found to be on the order of 10^2 monomer units per ns (approximately 1×10^2 UAs/ns), compared to a slowed growth rate in quiescent melt. A greater G means that after a nucleus passes n^*, it can integrate surrounding chains more rapidly, adding to the overall enhanced flow-induced crystallization.

It is also noteworthy that the induction times obtained from MFPT for the quiescent case ($\sim$ 241 ns) closely match the timescales estimated from the crystallinity curves (we earlier noted $\sim$240 ns from Figure 5.4). This agreement, just as in the flow case, reinforces the conclusion that our analysis is self-consistent. In both flow-induced and quiescent scenarios, the MFPT-derived τ^* values are essentially equal to the induction times identified by direct observation of $X_c(t)$, indicating that the MFPT method captures the same physical nucleation event timing as the raw simulation data. We can therefore be confident in the extracted kinetic parameters n^* and τ^* for both cases.

5.1.3 Nucleation Rate Calculations

The homogeneous nucleation rate I can be calculated using **Equation 4.9**. In this way, we computed the nucleation rates for the flow-induced and quiescent crystallization proto-

cols. For the **flow-induced case**, the induction time from the MFPT kinetic analysis is $\tau^* = 43.908 \pm 0.448$ ns, and the simulation cell volume of one system in the amorphous state—determined after rapid cooling and during the subsequent period of density equilibration—is $V = 2.763 \times 10^3$ nm^3. Converting to consistent units (seconds and cm^3) and substituting into the formula above, we obtain a nucleation rate of,

$$I_{\text{flow}} = (8.29 \pm 0.09) \times 10^{24} \text{ s}^{-1} \text{ cm}^{-3}. \tag{5.1}$$

For the **quiescent case**, the MFPT analysis yields a much longer induction time of $\tau^* = 241.25 \pm 1.20$ ns, for a similar simulation cell volume—$V = 2.763 \times 10^3$ nm^3. The corresponding nucleation rate in quiescent simulations is then,

$$I_{\text{quiescent}} = (1.51 \pm 0.01) \times 10^{24} \text{ s}^{-1} \text{ cm}^{-3}. \tag{5.2}$$

These calculations show that the flow-induced scenario has a significantly higher nucleation rate (on the order of 10^{24} s^{-1}cm^{-3}, about 5–6 times higher than the quiescent rate) due to the shorter induction time under flow. This practically means that, in the presence of an imposed flow, critical nuclei form at a much faster rate than under quiescent conditions.

5.1.4 Estimation of Induction Time from Probability Distributions of Nucleation Times

To rigorously test the induction time that we determined through the MFPT method, we also analyzed the statistical distribution of nucleation times for crystallization. This approach exploits the inherently stochastic nature of nucleation events; even when performed in fixed conditions, the time at which the first crystal (often referred to as a critical nucleus) appears varies from run to run. Following the method of Ter Horst and Jiang [89], we assume that the nucleation times follows a known two-parameter exponential cumulative distribution function. In particular, we use the assumption of a cumulative distribution of the form,

$$P(t) = 1 - \exp\left(-\frac{t - t_d}{\tau}\right) \tag{5.3}$$

where t_d is a correction term and τ controls how fast the process is happening once t_d has been achieved. A small value of τ means that the nucleation events are clustered around t_d, while a larger τ implies that nucleation times are broadly distributed. The induction time is thus defined by,

$$\tau^* = \tau + t_d \tag{5.4}$$

By fitting this theoretical distribution to our simulation data (the set of observed nucleation times across independent runs), we extracted the induction time τ^* parameter and compared it with our earlier MFPT results.

Using this distribution method, we calculated the induction times for flow-induced and quiescent crystallization protocols. **Figure 5.7** and **Figure 5.8** provide the cumulative induction time distribution from our simulations along with the best-fit theoretical curve. In the stretching conditions, the fitted induction time was roughly **44.95 ns**, which matched very well the MFPT-based induction time $\tau^* \approx 43.9$ ns.

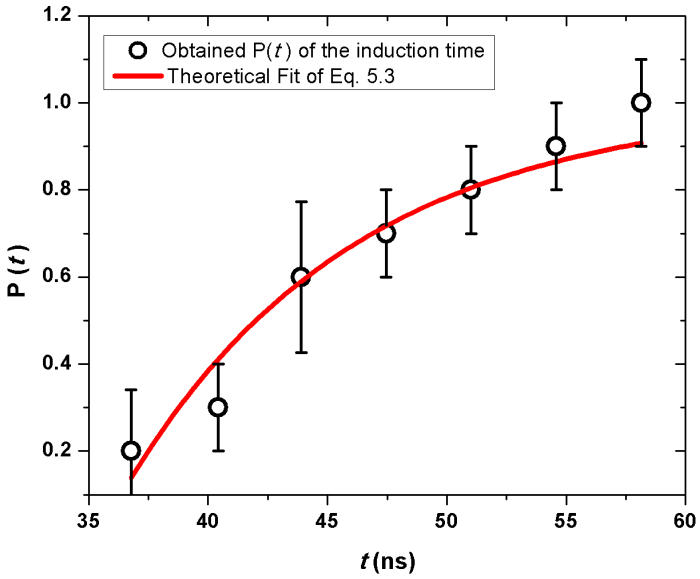


Figure 5.7: Obtained probability distribution P(t) of the induction time for 2K system in flow-induced conditions. The red solid line is a fit of the theoretical equation to the simulation data, while the open circles represent the binned values of nucleation times determined from MFPT analysis for each independent simulation (10 independent simulations). The error bars represent the standard error of each bin, estimated as $\sqrt{n}/N$, where n is the number of events in the bin and $N = 10$ is he number of independent simulations.

Analogously, under **quiescent conditions** (no flow), the distribution analysis gave an induction time of about **228.5 ns**, near the value of $\tau^* \approx 241.2$ ns calculated using the MFPT method. In other words, the same physical picture is found if one simply considers either the average kinetic trajectory or the statistical distribution of many independent nucleation events.

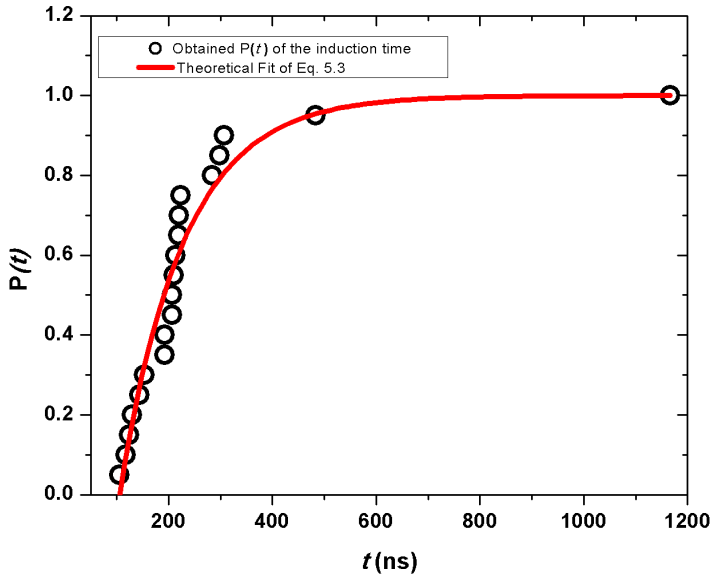


Figure 5.8: Obtained probability distribution P(t) of the induction time for 2K System in quiescent conditions. The red solid line is a fit of the theoretical equation to the simulation data, while the open circles represent the nucleation times determined from MFPT analysis for each independent simulation (20 independent simulations).

The good agreement between the induction times from distribution fitting and from the MFPT analysis (and also from direct observation of the $X_c(t)$ curves) reassures us that τ^* has correctly been determined as the true induction time.

5.1.5 Time Evolution of the Chain Root Mean Squared Radius of Gyration

Figure 5.9 shows how the chain root mean squared radius of gyration $\langle R_g^2 \rangle^{1/2}$ (black curve) and the Y-axis (transverse direction) simulation cell length (red line) change over time during the flow-induced crystallization of 2K PE system. The black curve increases almost linearly from 80 Å to 140 Å over time, while the Y-axis simulation cell length decreases in a similar trend from 140 Å to 80 Å. These trends reflect chain stretching and alignment. Experimental and simulation studies confirm that the flow field suppresses folded-chain pathways, favoring crystallization in stretched conformations that minimize entropic penalties and accelerate ordering.

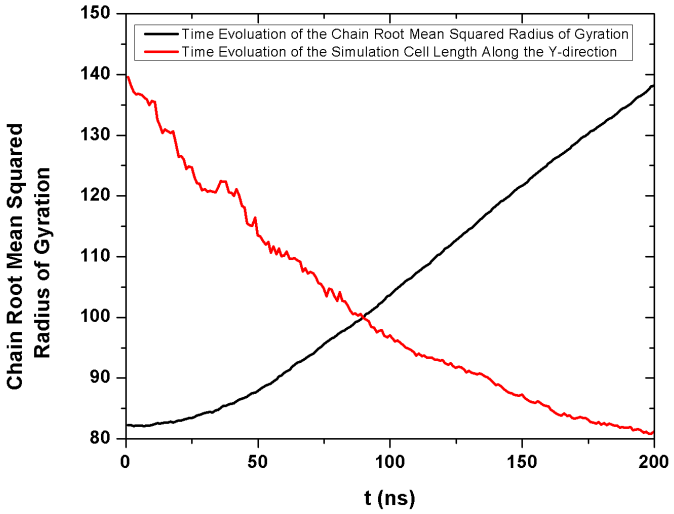


Figure 5.9: Time-dependent behavior of the chain root mean squared radius of gyration (black curve) and the simulation cell length along the Y-direction (red curve) for a 2K (C2000) PE system of polydispersity 1.08 crystallizing under flow-induced conditions at 340 K. The results shown are from one independent simulation.

In connection with Figure 5.9, Figure 5.10 shows the time-dependent behavior of the $\langle R_g^2 \rangle^{1/2}$ along with the dimensions of the simulation cell. The L_x increases linearly with time, indicating the direction of the uniaxial deformation, while L_y and L_z decrease, reflecting the reduced thickness as the drawing progresses.

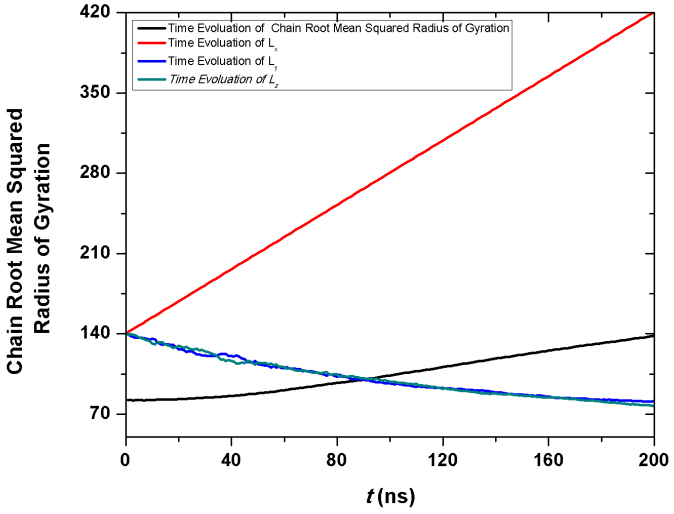


Figure 5.10: Time-dependent behavior of the chain root mean squared radius of gyration (black curve) and the simulation cell length along the X-, Y-, and Z-direction (red, blue and green curve, accordingly) for a 2K (C2000) PE system of polydispersity 1.08 crystallizing under flow-induced conditions at 340 K. The results shown are from one independent simulation.

Similarly, Figure 5.11 shows how the chain root mean squared radius of gyration (black curve) and the X-axis simulation cell length (red curve) change over time during quiescent crystallization of a 2K PE system. Both the black and the red curve remain almost constant around a mean value reflecting the conformational behavior of typical entangled polymer melts. In contrast with flow-induced scenarios, the chain root mean square of gyration does not exhibit a sharp rise, implying crystallization through classical chain-folding paths. Lastly, around 250-300 ns, a negligible upward trend in the black curve is probably due to the adoption of all-trans conformation by the stems inside the lamellae, while a downward trend in the red curve is related to the change in density due to crystallization.

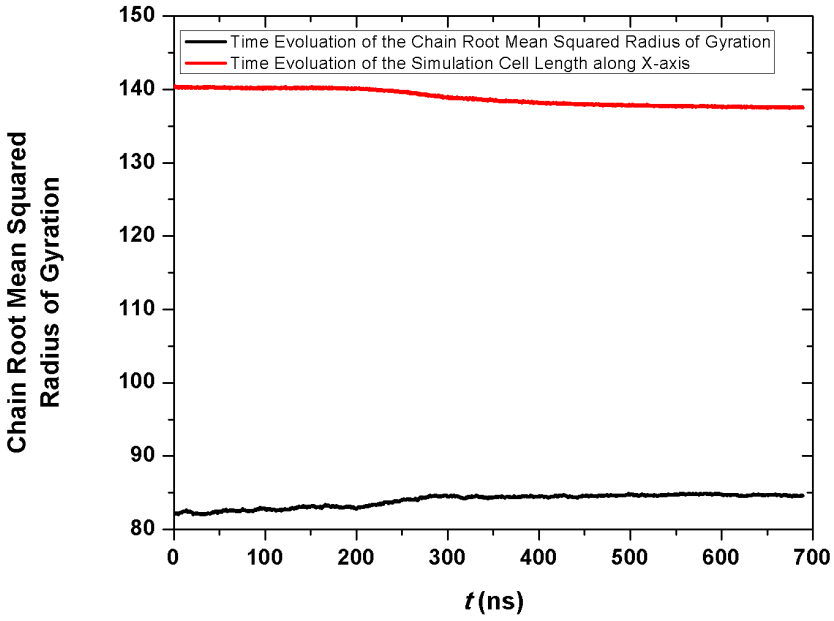


Figure 5.11: Chain root mean squared radius of gyration (black curve) and simulation cell length along the X-direction (red curve) for a 2K (C2000) PE system of polydispersity 1.08 in the absence of flow at 340 K. The results shown are from one independent simulation.

5.1.6 Crystallization Visualization

In this section, structural snapshots from the MD trajectories are provided in order to visualize how the crystallization processes in each scenario. For the case of flow-induced conditions, the polymer chains were initially aligned by the applied deformation, and the process of crystallization reflects this alignment. Four representative snapshots of the simulation cell (**Figure 5.12** to **Figure 5.15**) show the key stages of crystallization under flow. Initially (Figure 5.12), the entire simulation cell is amorphous, as indicated by the uniform pink coloring (with cyan reflecting crystalline regions). After a certain delay equal to the induction time, the first tiny crystalline regions begin to form. At time $t \approx \tau^*$, we observe the appearance of one or more green patches, indicating that a critical-size nucleus has been created in the amorphous matrix (Figure 5.13). Once this nucleus emerges, crystallization

occurs at a fast rate, the small crystallites grow, and other crystallites may form largely oriented along the stretch direction. In an intermediate snapshot (Figure 5.14), the crystalline regions have developed, showing clearly the alignment of chains due to flow. Finally, in the later stage (Figure 5.15), a substantial majority of the simulation cell has crystallized. At the last frame of the simulation, approximately half of the cell is cyan colored, which means that a very large percentage of the amorphous material has become crystallized into an ordered, oriented structure.

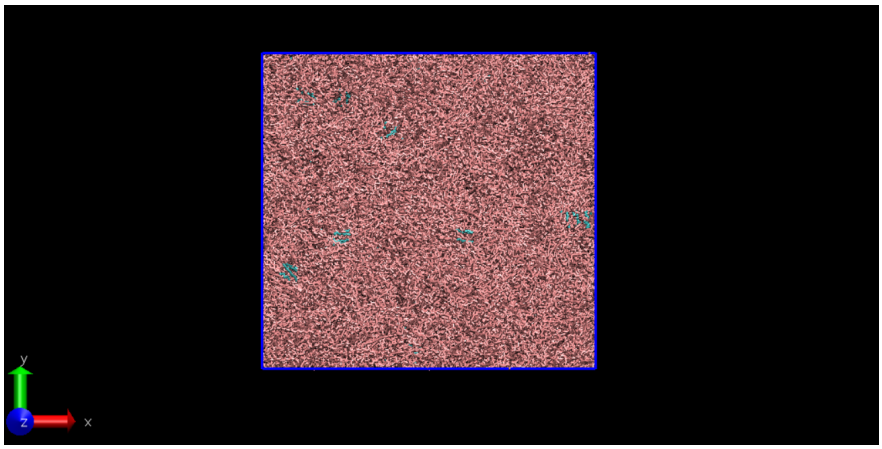


Figure 5.12: Initial configuration of the 2K PE system at $t \approx 0\,\text{ns}$ after quenching to 340 K under flow-induced conditions. Pink amorphous regions ($P_2 < 0.7$).

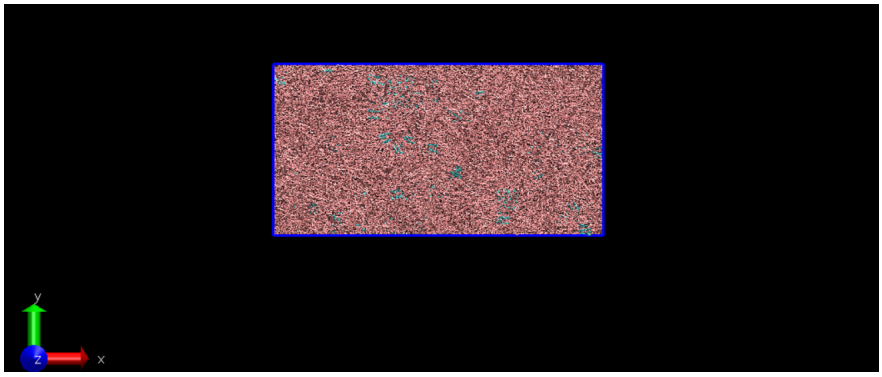


Figure 5.13: Emergence of a critical nucleus at $t \approx \tau^*$ during uniaxial elongation ($\dot{\varepsilon} = 10^7\ \text{s}^{-1}$) of the 2K PE system. Cyan crystalline regions ($P_2 > 0.7$)

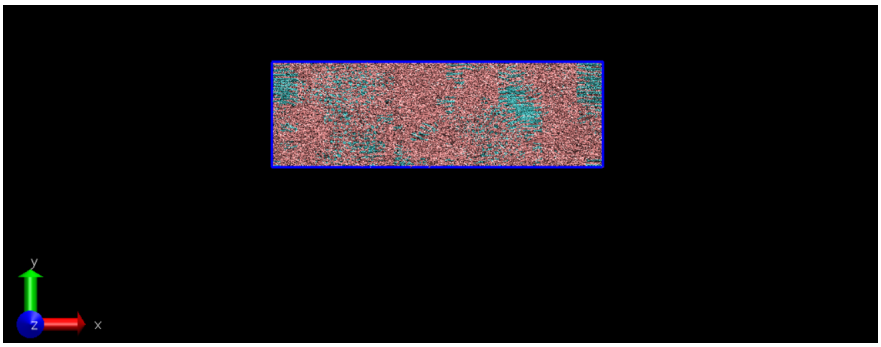


Figure 5.14: Intermediate crystallization stage under flow.

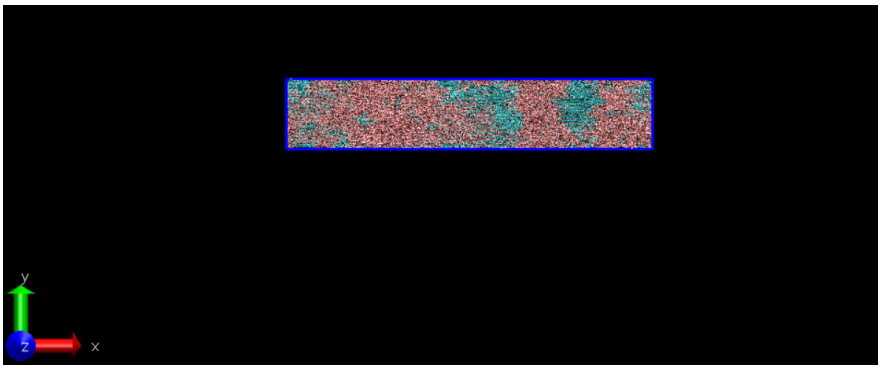


Figure 5.15: Final oriented semi-crystalline morphology ($t = 200\,\text{ns}$) under flow-induced conditions.

On the other hand, when in **under quiescent conditions** (no flow is applied), the crystallization follows a different visual pathway. Snapshots of a quiescent simulation (**Figure 5.16** to **Figure 5.19**) show that, in the beginning, the system is entirely amorphous (Figure 5.16, all pink, no cyan). But, without any flow to pre-align or to disentangle the chains, the polymer melt remains in an entangled state for a much longer time. The first crystal nucleus exists only after a prolonged waiting time and at some random location in the simulation cell. Once a stable nucleus finally forms, it begins to grow outwards in all directions into the surrounding melt. The new crystallite grows to become a lamella that expands roughly radially from the nucleation site. As the simulation goes on further, additional nuclei emerge independently in other regions of the simulation cell. Throughout the quiescent crystallization, at no point do we observe any global alignment of the crystal; instead, each crystalline region is oriented differently. The final snapshots (Figure 5.19) of a quiescent run show several such crystallized regions (cyan) distributed among the amorphous (pink) matrix, without a predominant orientation visible between the crystallites.

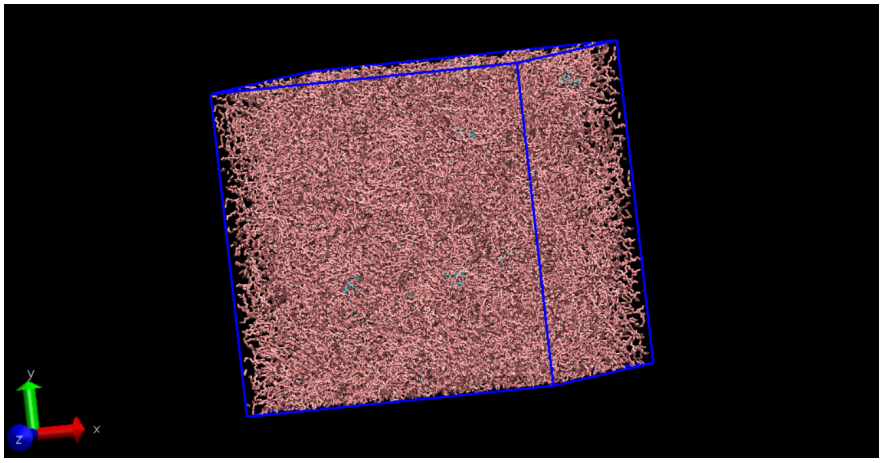


Figure 5.16: Initial amorphous configuration of the 2K PE system under quiescent conditions at $t = 0$ns (340K). Pink amorphous regions ($P_2 < 0.7$).

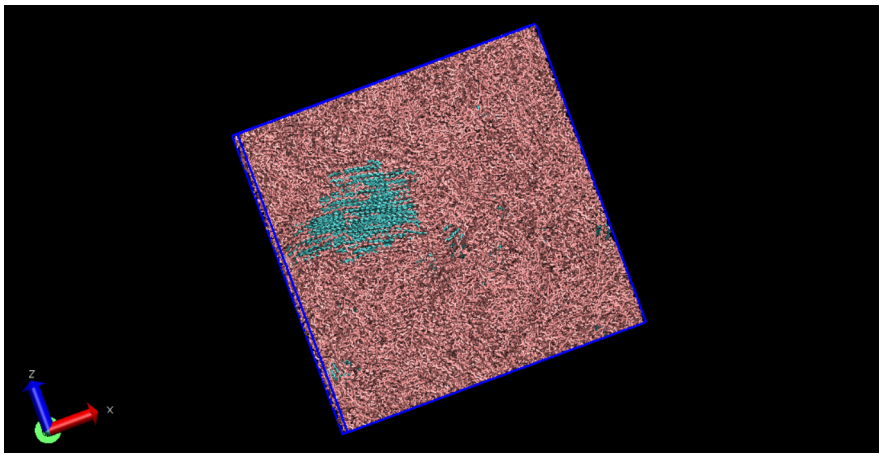


Figure 5.17: Critical nucleus formation at $t \approx 240$ns in quiescent crystallization. Cyan crystalline regions ($P_2 > 0.7$)

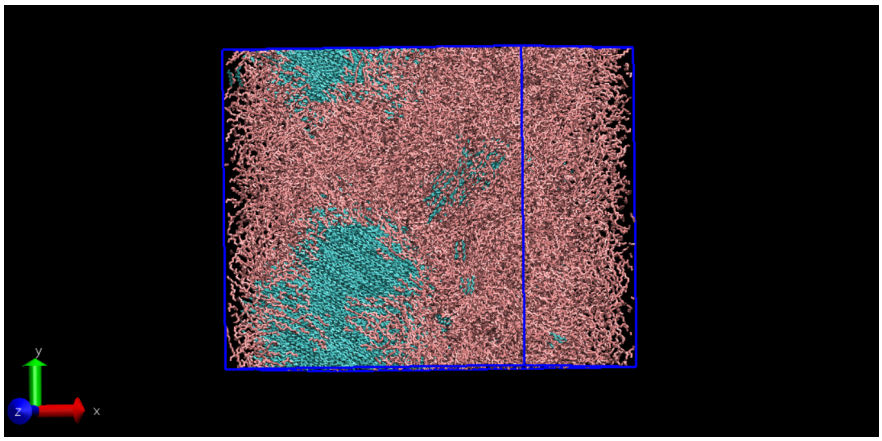


Figure 5.18: Intermediate crystallization stage under quiescent conditions.

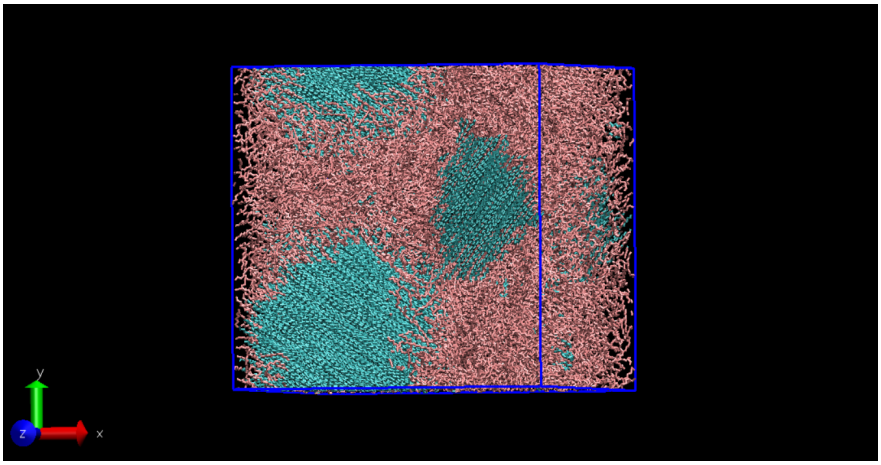


Figure 5.19: Final semi-crystalline morphology from quiescent crystallization. Multiple independent crystals (cyan) with random crystallographic orientations are formed by the end of the simulation.

5.2 Molecular Weight Effects on Crystallization: 1K vs. 2K Systems

Having characterized the crystallization kinetics for 2K PE melt (50 chains with an average of 2,000 CH_2 units per chain), a comparison was made between these results and those of a lower-molecular-weight **1K system** studied by Anogiannakis and Venetsanos (100 chains with 1,000 CH_2 units per chain). This comparison allows us to isolate the influence of **molecular weight (M_w)** on crystal nucleation and growth under identical thermodynamic conditions.

5.2.1 Flow-Induced Conditions

Figure 5.20 summarizes the degree of crystallinity evolution for the 1K system under flow, based on 21 independent simulations. Under flow-induced crystallization, the 1K and 2K systems exhibit virtually the same behavior. The individual degree of crystallinity vs. time curves for the 1K case all collapse onto a narrow band (similar to our Figure 5.1 for the 2K case), indicating very little run-to-run variation in nucleation timing. Quantitatively, the induction time for the 1K system under flow is around $\tau^* \approx 45$ ns, essentially identical to the induction time ($\approx 45ns$) we found for the 2K system. Thus, within the accuracy of our measurements, **molecular weight has no discernible effect on the crystallization kinetics in strong extensional flow**. This makes sense, at the high strain rate applied $\dot{\varepsilon} = 10^7$ s^{-1}, even the longer chains in the 2K melt are strongly stretched and oriented, so both 1K and 2K melts nucleate rapidly. The flow overrides subtle differences in chain length by aligning any sufficiently long polymer to promote nucleation.

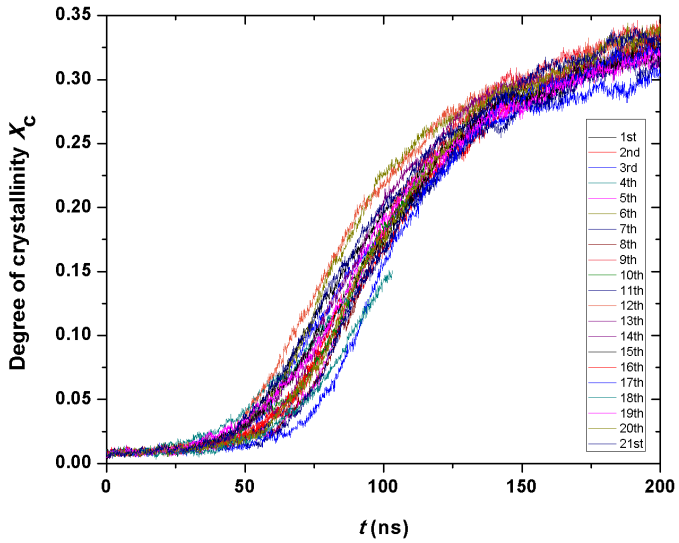


Figure 5.20: Time evolution of the degree of Crystallinity X_c from 21 independent MD simulations of polydisperse 1K PE system under stretching conditions. Flow significantly reduces the induction time and narrows trajectory dispersion compared to quenching.

5.2.2 Quiescent Conditions

Quiescent crystallization paints a similar picture. **Figure 5.21** shows the crystallinity vs. time results for the 1K system (23 independent quiescent simulations). In the absence of flow, there is significant variability in the induction times. Importantly, the overall spread and trend are comparable between 1K and 2K. The 1K system's nucleation times are "better" broadly distributed compared to 2K system's nucleation times, but the induction time is one the same order as that of 2K system. We estimate an induction time of roughly 293-295 ns for the 1K melt, whereas the 2K melt's induction time was about 240-245 ns. Given the statistical uncertainties (each data set has a finite number of samples), these values are very close. In fact, the small 40-50 ns difference is likely not significant. Our 2K simulations had a gap in nucleation events between $\approx 500 - 1100$ns simply due to the limited sampling (20 independent simulations), whereas the 1K study, with more runs, filled in that time range. With an additional 2K simulations, one would expect the induction time to converge further. Thus, **under quiescent conditions, we again observe no strong influence of chain length on crystallization kinetics**, a two-fold increase in M_w (and the associated increase in chain entanglements) did not measurably delay the onset of crystallization in our simulations.

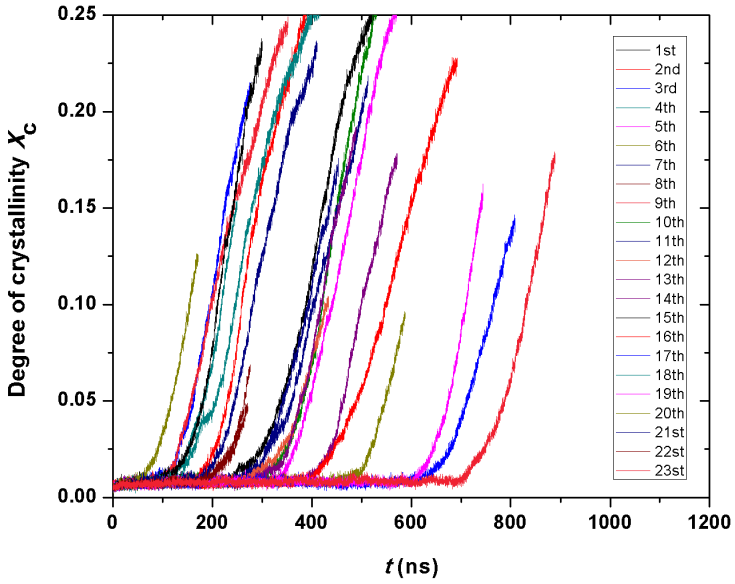


Figure 5.21: Time-resolved crystallinity trajectories $X_c(t)$ from 23 independent MD simulations of polydisperse 1K PE system under quiescent conditions. Each $X_c(t)$ reflects the stochastic nature of homogeneous nucleation, with the induction time for nucleation varying significantly across runs.

The absence of a significant molecular weight effect in both protocols suggests that, at least under the conditions examined (T=340K, chains well in the entangled regime), the crystallization rate is primarily controlled by factors other than chain length. Under flow, the dominant factor is the applied deformation, which orients chains and greatly accelerates nucleation irrespective of molar mass. Under quiescent conditions, the kinetics are slow for both melts, governed by the necessity of a rare thermal fluctuation to overcome the nucleation barrier, a process that is inherently sluggish whether the chains are 1K or 2K in length. Our findings here are in line with classic experimental studies on PE crystallization. **Ergoz, Fatou & Mandelkern** [90] investigated a broad range of linear PE molecular weights and found that higher weight average molar mass M_w generally slows down crystallization, but only to a modest degree. In their data, the overall crystallization rate decreased moderately as M_w increased, especially at shallow subcoolings; at very high subcoolings (where nucleation is fast for all cases), the effect of molecular weight was not dramatic. Our simulation results mirror this behavior–at the deep subcooling of 340K (which is tens of degrees under the melting temperature for PE), the difference between a 1K and 2K melt is minimal–both are highly subcooled and thus crystallize fast, but at nearly the same rate. We therefore conclude that molecular weight differences (within the studied range) do not strongly affect the nucleation kinetics under our conditions. Any slight trends (e.g., the 2K system appearing faster in quiescent nucleation) are likely due to the statistical scatter. Indeed, if anything, our comparison hints that entanglements in the higher M_w system did not provide any extra hindrance to nucleation on the timescale observed. Both systems are sufficiently long and possess a well-developed entanglement network. It should be noted, however, that at higher

temperatures (i.e, lower degrees of subcooling) one would expect molecular weight to play a larger role–longer chains would then crystallize noticeably more slowly due to entanglement constraints, as reported in experiments. In the extreme flow case here, even a high M_w does not impede crystallization because the flow effectively "melts" away the entanglement network by aligning the chains.

5.2.3 MFPT-Derived Kinetic Parameters

In this subsection, we compare the kinetic parameters obtained for each crystallization protocol from the MFPT analysis for both 1K and 2K systems. Table 5.3 present MFPT-derived crystallization parameters for the 1K PE system under stretching and quiescent conditions. The values were provided through Dr. Anogiannakis and Mr. Venetsanos, who performed the 1K simulations. **(Once more, it should be mentioned that the work of this thesis is the 2K system; the 1K data are provided here for the sake of comparison only).**

	Flow-Induced Crystallization	**Quiescent Crystallization**
τ^* (ns)	43.64 ± 0.35	297.68 ± 1.20
G (UAs/ns)	111.51 ± 2.53	85.55 ± 1.54
n^* (UAs)	105.71 ± 2.46	99.39 ± 3.81
Z	$0.00368 \pm 1.42 \times 10^{-4}$	$0.00174 \pm 6.70 \times 10^{-5}$

Table 5.3: Mean values of induction time (τ^*), growth rate (G), critical nucleus size (n^*), and Zeldovich factor (Z) for the 1K PE system under two crystallization protocols. Under flow-induced conditions, 21 independent simulations were conducted at 340K and $\dot{\epsilon} = 10^7$ s^{-1}, while under quiescent conditions, 23 independent simulations were conducted at 340K.

Most significantly, the induction time τ^* and the critical nucleus size n^* for 1K during stretching are essentially identical as we found for 2K ($\tau^* \approx 44$ns, $n^* \approx 107$). This suggests that **molecular weight has minimal influence on nucleation kinetics under intense flow**. For the second crystallization protocol, the MFPT induction time is $\tau^* \approx 295$ns, only slightly longer than 2K's values. Given the uncertainties and the sampling issues discussed above, we do not put significant emphasis on the small differences between 1K and 2K.

The general conclusion is that the overall crystallization rates and thermodynamic barrier (indicated by τ^* and n^*) are very close to each other for the two studied molecular weights at 340 K.

Chapter 6

Conclusion & Future Work

6.1 Conclusion

This work employs molecular simulation methods to investigate the crystallization kinetic behavior of two different polydisperse polyethylene melt systems under quiescent and flow-induced conditions while also varying the average molecular weight. The key findings can be summarized as follows.

The existence of strong uniaxial flow on the polymer melt accelerates dramatically the kinetics of crystallization. Specifically, the induction time τ^* was on the order of 44 ns, compared to approximately 240 ns under quiescent conditions for the same temperature and polymer system. This trend is attributed to the orientational ordering of the chains, as external deformation promotes frequent, quasi-one-dimensional contact between chains, which lowers the kinetic barrier for generating a nucleus with critical size. As a result, the calculated nucleation rate I in the stretched system was about $5\times$ higher than in the quiescent system, in accordance with the reduced induction time. On the other hand, the critical nucleus size n^* was calculated to be of the same order of magnitude in both cases (on the order of 10^2 methylene units). For MFPT analysis, a critical nucleus size $n^* \approx 107$ UAs in the stretched case was calculated compared to $n^* \approx 102$ UAs in the quiescent case. This suggests that flow affect mostly the kinetics of nucleation (by shortening the time needed to form a supercritical nucleus) without fundamentally altering the thermodynamics.

Additionally, negligible molecular weight dependence was found within the studied range (C1000 vs C2000 chains). For both quiescent and flow conditions, the two systems exhibited almost identical nucleation behavior. Any minor discrepancies found were not significant, indicating that at 340K, the chain length effect on homogeneous nucleation kinetics is small, which is most likely due to the fact that the simulations were conducted at constant deep subcooling, where restrictions on chain mobility dominate chain length differences.

Overall, the Thesis provides molecular-level evidence that flow-induced nucleation can highly accelerate PE crystallization with little impact on the critical nucleus size, and within a certain regime, molecular weight is of little consequence for nucleation at a given subcooling. These findings provide a clue on our fundamental understanding of polymer crystallization under two different crystallization protocols, one of which is part of an industry process, giving us an insight into designing processing procedures to obtain desired crystalline microstructures in semi-crystalline polymers.

6.2 Future Work

Having this study as a reference point, there are numerous directions that arise for future study

6.2.1 Effect of Higher Temperature (Lower Subcooling)

All MD simulations in this study were carried out at 340K, a relatively low temperature for PE, which facilitates rapid nucleation. Future works can examine higher temperatures and investigate whether Molecular Weight plays a more significant role in the kinetics of crystallization compared to our results.

6.2.2 Varying Flow Strength and Partial Alignment

A high strain rate was used throughout this study to induce alignment. Future research can investigate a range of flow or shear rates to outline the correlation of the degree of chain alignment with the nucleation rate. Using weaker flows or considering a partially aligned initial state, one might find the threshold of orientational order.

6.2.3 Effect of Larger Dispersities and Molecular Architecture

Lastly, future research could investigate systems with very large dispersities, such as those found in industrial materials. Another direction would be to investigate more complex molecular architectures, such as short- and long-chain branching, as found in LLDPE and LDPE.

Bibliography

[1] PlasticsEurope. Plastics-the facts 2022: An analysis of european plastics production, demand and waste data, 2022. Brussels, Belgium.

[2] Takashi Yamamoto. Computer modeling of polymer crystallization – toward computer-assisted materials' design. *Polymer*, 50(9):1975–1985, 2009.

[3] Alexander J. Bourque. Molecular modeling of polymer crystallization and the effect of nucleating agents. 2017.

[4] Ewa Piorkowska and Gregory C. Rutledge. *Handbook of Polymer Crystallization*. Wiley, 2013.

[5] ADMIRE. Admire - youtube channel. https://www.youtube.com/@ADMIRE1, 2025. Accessed: 2025-06-16.

[6] Dimitrios-Paraskevas Gerakinis. Generation of polymeric melt models with predefined molecular-weight distributions employing monte carlo atomistic simulations. Master's thesis, National Technical University of Athens, School of Chemical Engineering, Athens, Greece, July 2022.

[7] Doros Theodorou. Notes on molecular simulation. http://comse.chemeng.ntua.gr/files/MS_notes.pdf, n.d. School of Chemical Engineering, National Technical University of Athens.

[8] T. Isaac. Periodic boundary conditions. https://isaacs.sourceforge.io/phys/pbc.html, 2025. Accessed: 2025-06-16.

[9] A. L. Andrady and M. A. Neal. Applications and societal benefits of plastics. *Philosophical Transactions of the Royal Society B: Biological Sciences*, 364(1526):1977, 2009.

[10] Ulf W. Gedde. *Polymer Physics*. Springer Dordrecht, Dordrecht, Netherlands, 1 edition, 1999.

[11] Goran Ungar and Xiang-Bing Zeng. Learning polymer crystallization with the aid of linear, branched and cyclic model compounds. *Chemical Reviews*, 101(12):4157 – 4188, 2001. Cited by: 167.

[12] Essential Chemical Industry. Polyethene, 2025. Accessed: 27-Feb-2025.

[13] Woldemar d'Ambrières. Plastics recycling worldwide: current overview and desirable changes. *Field Actions Science Reports*, Special Issue 19:12–21, 2019.

[14] C. B. Kaufmann. Leo h. baekeland. In *ACS Symposium Series*, volume 1080, pages 1–10. American Chemical Society, 2011.

[15] Roland Geyer, Jenna R. Jambeck, and Kara Lavender Law. Production, use, and fate of all plastics ever made. *Science Advances*, 3:e1700782, 2017.

[16] I. Ignatyev, W. Thielemans, and Bob Vander Beke. Recycling of polymers: a review. *ChemSusChem*, 2014.

[17] Z. Wen, Y. Xie, M. Chen, et al. China's plastic import ban increases prospects of environmental impact mitigation of plastic waste trade flow worldwide. *Nature Communications*, 12:425, 2021.

[18] Hidayah, Nurul and Syafrudin. A review on landfill management in the utilization of plastic waste as an alternative fuel. *E3S Web Conf.*, 31:05013, 2018.

[19] Luke Makarichi, Warangkana Jutidamrongphan, and Kua anan Techato. The evolution of waste-to-energy incineration: A review. *Renewable and Sustainable Energy Reviews*, 91:812–821, 2018.

[20] Timmy Thiounn and Rhett C. Smith. Advances and approaches for chemical recycling of plastic waste. *Journal of Polymer Science*, 58(10):1347–1364, 2020.

[21] Zoé O. G. Schyns and Michael P. Shaver. Mechanical recycling of packaging plastics: A review. *Macromolecular Rapid Communications*, 42(3):2000415, 2021.

[22] Rashid Miandad, Mohammad Rehan, Mohammad A. Barakat, Asad S. Aburiazaiza, Hizbullah Khan, Iqbal M. I. Ismail, Jeya Dhavamani, Jabbar Gardy, Ali Hassanpour, and Abdul-Sattar Nizami. Catalytic pyrolysis of plastic waste: Moving toward pyrolysis based biorefineries. *Frontiers in Energy Research*, 7, 2019.

[23] Alicia Aguado, L. Martínez, L. Becerra, M. Arieta-Araunabeña, S. Arnaiz, A. Asueta, and I. Robertson. Chemical depolymerisation of pet complex waste: hydrolysis vs. glycolysis. *Journal of Material Cycles and Waste Management*, 16(2):201–210, 2014.

[24] J. Lange and Yves Wyser. Recent innovations in barrier technologies for plastic packaging—a review. *Packaging Technology and Science*, 16(4):149–158, 2003.

[25] K. Kaiser, M. Schmid, and M. Schlummer. Recycling of polymer-based multilayer packaging: A review. *Recycling*, 3(1):1, 2018.

[26] Borstar®-based full pe laminate solution improves recyclability of flexible packaging materials. Available online, 2016. Accessed on 27 February 2025.

[27] Muhammad Anwar, Joshua T. Berryman, and Tanja Schilling. Crystal nucleation mechanism in melts of short polymer chains under quiescent conditions and under shear flow. *The Journal of Chemical Physics*, 141(12):124910, 09 2014.

[28] Wenlin Zhang and Ronald G. Larson. Effect of flow-induced nematic order on polyethylene crystal nucleation. *Macromolecules*, 53(18):7650–7657, 2020.

[29] Seyed H. Tabatabaei, Laurent R Parent, Patrick Cigana, Abdellah Ajji, and Pierre J. Carreau. Effect of machine direction orientation conditions on properties of hdpe films. *Journal of Plastic Film & Sheeting*, 25:235 – 249, 2009.

[30] Tirtha Chatterjee, Rajen Patel, John Garnett, Rajesh Paradkar, Shouren Ge, Lizhi Liu, Kenneth T. Forziati, and Nik Shah. Machine direction orientation of high density polyethylene (hdpe): Barrier and optical properties. *Polymer*, 55(16):4102–4115, 2014. Polymerized Ionic Liquids.

[31] Stefanos D. Anogiannakis, Fotis Venetsanos, and Doros N. Theodorou. Simulating stretch-induced crystallization of polyethylene films: Strain rate and temperature effect on the kinetics and morphology. *Macromolecules*, 57(15):7331–7346, 2024.

[32] Nikolaos I. Sigalas, Stan A. T. Van Kraaij, and Alexey V. Lyulin. Effect of temperature on flow-induced crystallization of isotactic polypropylene: A molecular-dynamics study. *Macromolecules*, 56(21):8417–8427, 2023.

[33] Günter Reiter and Gert Strobl. *Progress in Understanding of Polymer Crystallization*, volume 714. 01 2007.

[34] Z. Bartczak. Deformation of semicrystalline polymers – the contribution of crystalline and amorphous phases. *Polimery*, 62(11-12):787–799, Jan. 2021.

[35] John D. Hoffman and Robert L. Miller. Kinetic of crystallization from the melt and chain folding in polyethylene fractions revisited: theory and experiment. *Polymer*, 38(13):3151–3212, 1997.

[36] G. W. Greenwood, A. L. Greer, D. M. Herlach, K. F. Kelton, and M. Muthukumar. Molecular modelling of nucleation in polymers. *Philosophical Transactions of the Royal Society of London. Series A: Mathematical, Physical and Engineering Sciences*, 361(1804):539–556, 2003.

[37] Gert Strobl. Crystallization and melting of bulk polymers: New observations, conclusions and a thermodynamic scheme. *Progress in Polymer Science*, 31(4):398–442, 2006.

[38] Peng Yi, C. Rebecca Locker, and Gregory C. Rutledge. Molecular dynamics simulation of homogeneous crystal nucleation in polyethylene. *Macromolecules*, 46(11):4723–4733, 2013.

[39] Peng Yi and Gregory C. Rutledge. Molecular simulation of crystal nucleation in n-octane melts. *The Journal of Chemical Physics*, 131(13):134902, 10 2009.

[40] C. Schick, R. Androsch, and J. W. P. Schmelzer. Homogeneous crystal nucleation in polymers. *Journal of Physics: Condensed Matter*, 29(45):453002, 2017.

[41] Kyle Wm. Hall, Timothy W. Sirk, Simona Percec, Michael L. Klein, and Wataru Shinoda. Monodisperse polymer melts crystallize via structurally polydisperse nanoscale clusters: Insights from polyethylene. *Polymers*, 12(2), 2020.

[42] Kiyoka Okada, Kaori Watanabe, Isao Wataoka, Akihiko Toda, Sono Sasaki, Katsuaki Inoue, and Masamichi Hikosaka. Size distribution and shape of nano-nucleus of polyethylene simultaneously determined by saxs. *Polymer*, 48:382–392, 2007.

[43] K.F. Kelton. Crystal nucleation in liquids and glasses. volume 45 of *Solid State Physics*, pages 75–177. Academic Press, 1991.

[44] J. W. Gibbs. *The Collected Works of J. Willard Gibbs*, volume 1. Longmans, Green and Co., New York, 1928.

[45] V. Volmer and A. Weber. Nucleus formation in supersaturated systems. *Z. Phys. Chem.*, 119:277, 1926.

[46] R. Becker and W. Döring. *Ann. Phys.*, 24:719, 1935.

[47] J. B. Zeldovich. *Acta Physicochim. USSR*, 18:1, 1943.

[48] D. Kashchiev. *Nucleation: Basic Theory with Applications*. Butterworth Heinemann, Oxford, 2000.

[49] T. Verho, A. Paajanen, J. Vaari, and A. Laukkanen. Crystal growth in polyethylene by molecular dynamics: The crystal edge and lamellar thickness. *Macromolecules*, 51(13):4865–4873, 2018.

[50] K. W. Hall, T. W. Sirk, S. Percec, M. L. Klein, and W. Shinoda. Divining the shape of nascent polymer crystal nuclei. *The Journal of Chemical Physics*, 151(14):144901, 2019.

[51] Renkuan Cao, Fan Peng, Yunhan Zhang, Hao Sun, Ziwei Liu, Tingyu Xu, and Liangbin Li. Entropy-driven preordering assists nucleation in polyethylene. *Polymer*, 323:128179, 2025.

[52] David W. Oxtoby. Nucleation of first-order phase transitions. *Accounts of Chemical Research*, 31(2):91–97, 1998.

[53] David W. Oxtoby and Dimo Kashchiev. A general relation between the nucleation work and the size of the nucleus in multicomponent nucleation. *The Journal of Chemical Physics*, 100(10):7665–7671, 05 1994.

[54] Peter Harrowell and David W. Oxtoby. A molecular theory of crystal nucleation from the melt. *The Journal of Chemical Physics*, 80(4):1639–1646, 02 1984.

[55] Takashi Yamamoto. Molecular dynamics simulations of steady-state crystal growth and homogeneous nucleation in polyethylene-like polymer. *The Journal of Chemical Physics*, 129(18):184903, 11 2008.

[56] Chuanfu Luo and Jens-Uwe Sommer. Growth pathway and precursor states in single lamellar crystallization: Md simulations. *Macromolecules*, 44(6):1523–1529, 2011.

[57] Jens-Uwe Sommer and Günter Reiter. Polymer crystallization in quasi-two dimensions. ii. kinetic models and computer simulations. *The Journal of Chemical Physics*, 112(9):4384–4393, 03 2000.

[58] Xiaoliang Tang, Fucheng Tian, Tingyu Xu, Liangbin Li, and Aleks Reinhardt. Numerical calculation of free-energy barriers for entangled polymer nucleation. *The Journal of chemical physics*, 152 22:224904, 2020.

[59] Xiaoliang Tang, Junsheng Yang, Tingyu Xu, Fucheng Tian, Chun Xie, and Liangbin Li. Local structure order assisted two-step crystal nucleation in polyethylene. *Physical Review Materials*, 1, 2017.

[60] Wenbing Hu and Tao Cai. Regime transitions of polymer crystal growth rates: molecular simulations and interpretation beyond lauritzen-hoffman model. *Macromolecules*, 41(6):2049–2061, 2008.

[61] Xiaoming Jiang, Günter Reiter, and Wenbing Hu. How chain-folding crystal growth determines the thermodynamic stability of polymer crystals. *The Journal of Physical Chemistry B*, 120(3):566–571, 2016. PMID: 26720595.

[62] Wenbing Hu. Chain folding in polymer melt crystallization studied by dynamic monte carlo simulations. *The Journal of Chemical Physics*, 115(9):4395–4401, 09 2001.

[63] Mingqiu Wang, Huanhuan Gao, Liyun Zha, Er-Qiang Chen, and Wenbing Hu. Systematic kinetic analysis on monolayer lamellar crystal thickening via chain-sliding diffusion of polymers. *Macromolecules*, 46(1):164–171, 2013.

[64] Nikos Ch. Karayiannis, Katerina Foteinopoulou, and Manuel Laso. Entropy-driven crystallization in dense systems of athermal chain molecules. *Phys. Rev. Lett.*, 103:045703, Jul 2009.

[65] Katerina Foteinopoulou, Nikos Ch. Karayiannis, and Manuel Laso. Monte carlo simulations of densely-packed athermal polymers in the bulk and under confinement. *Chemical Engineering Science*, 121:118–132, 2015. 2013 Danckwerts Special Issue on Molecular Modelling in Chemical Engineering.

[66] David A. Nicholson and Gregory C. Rutledge. Molecular simulation of flow-enhanced nucleation in n-eicosane melts under steady shear and uniaxial extension. *The Journal of Chemical Physics*, 145(24):244903, 12 2016.

[67] Georgios Vogiatzis. *Multiscale Simulations of Polymer-Matrix Nanocomposites*. PhD thesis, School of Chemical Engineering, National Technical University of Athens, Athens, Greece, 2015.

[68] Jan von Plato. Boltzmann's ergodic hypothesis. *Archive for History of Exact Sciences*, 42(1):71–89, 1991.

[69] GROMACS Development Team. *GROMACS User Manual*. GROMACS, 2025. Version 2025, retrieved from https://manual.gromacs.org/.

[70] Michael P. Allen and Dominic J. Tildesley. *Computer Simulation of Liquids*. Oxford University Press, London, England, 2 edition, 2017.

[71] Godehard Sutmann. Classical molecular dynamics. In Jürgen Grotendorst, Dominik Marx, and Alejandro Muramatsu, editors, *Quantum Simulations of Complex Many-Body Systems: From Theory to Algorithms*, volume 10 of *NIC Series*, pages 211–254. John von Neumann Institute for Computing, Jülich, Germany, 2002.

[72] Scienomics. Optimizing packaging material using maps lammps plugin. https://www.scienomics.com/case-studies/optimizing-packaging-material/, n.d. Accessed: 2025-04-21.

[73] D. N. Theodorou and U. W. Suter. Detailed molecular structure of a vinyl polymer glass. *Macromolecules*, 18:1467–1478, 1985.

[74] D. C. Rapaport. *The Art of Molecular Dynamics Simulation*. Cambridge University Press, USA, 1995.

[75] Ya-Pu Zhao, Feng-Chao Wang, and Mei Chi. *Molecular Dynamics Simulation and Molecular Orbital Method*, pages 1559–1595. Springer International Publishing, Cham, 2018.

[76] Siepmann Group. Trappe force field: Transferable potentials for phase equilibria. http://trappe.oit.umn.edu/. Accessed: 2025-04-21.

[77] Mathias Pütz, John G. Curro, and Gary S. Grest. Self-consistent integral equation theory for polyolefins: Comparison to molecular dynamics simulations and x-ray scattering. *The Journal of Chemical Physics*, 114(6):2847–2860, 02 2001.

[78] William L. Jorgensen, David S. Maxwell, and Julian Tirado-Rives. Development and testing of the opls all-atom force field on conformational energetics and properties of organic liquids. *Journal of the American Chemical Society*, 118(45):11225–11236, 1996.

[79] H. Sun. Compass: An ab initio force-field optimized for condensed-phase applications overview with details on alkane and benzene compounds. *The Journal of Physical Chemistry B*, 102(38):7338–7364, 1998.

[80] GROMOS Development Team. Gromos: The groningen molecular simulation software. https://www.gromos.net/. Accessed: 2025-04-21.

[81] Marcus G. Martin and J. Ilja Siepmann. Transferable potentials for phase equilibria. 1. united-atom description of n-alkanes. *The Journal of Physical Chemistry B*, 102(14):2569–2577, 1998.

[82] Javier Ramos, Loukas D. Peristeras, and Doros N. Theodorou. Monte carlo simulation of short chain branched polyolefins in the molten state. *Macromolecules*, 40(26):9640–9650, 2007.

[83] Javier Ramos, Juan F. Vega, and Javier Martínez-Salazar. Molecular dynamics simulations for the description of experimental molecular conformation, melt dynamics, and phase transitions in polyethylene. *Macromolecules*, 48(14):5016–5027, 2015.

[84] Marc S. Lavine, Numan Waheed, and Gregory C. Rutledge. Molecular dynamics simulation of orientation and crystallization of polyethylene during uniaxial extension. *Polymer*, 44(5):1771–1779, 2003.

[85] Min Jae Ko, Numan Waheed, Marc S. Lavine, and Gregory C. Rutledge. Characterization of polyethylene crystallization from an oriented melt by molecular dynamics simulation. *The Journal of Chemical Physics*, 121(6):2823–2832, 08 2004.

[86] D. P. Gerakinis, S. D. Anogiannakis, and D. N. Theodorou. Equilibration of linear polyethylene melts with pre-defined molecular weight distributions employing united atom monte carlo simulations. *The Journal of Chemical Physics*, 161(4):044901, 2024.

[87] Takashi Yamamoto. Molecular dynamics simulation of stretch-induced crystallization in polyethylene: Emergence of fiber structure and molecular network. *Macromolecules*, 52(4):1695–1706, 2019.

[88] Jan Wedekind, Reinhard Strey, and David Reguera. New method to analyze simulations of activated processes. *The Journal of Chemical Physics*, 126(13):134103, 04 2007.

[89] Shanfeng Jiang and Joop H. ter Horst. Crystal nucleation rates from probability distributions of induction times. *Crystal Growth & Design*, 11(1):256–261, 2011.

[90] E. Ergoz, J. G. Fatou, and L. Mandelkern. Molecular weight dependence of the crystallization kinetics of linear polyethylene. i. experimental results. *Macromolecules*, 5(2):147–157, 1972.